Benchmarking a quantum computer using an engineered dissipative steady-state

Yigal Ilin^{1*} and Itai Arad^{2,3}

¹ Andrew and Erna Viterbi Department of Electrical and Computer Engineering,

Technion – Israel Institute of Technology, 3200003, Haifa, Israel

² Physics Department, Technion – Israel Institute of Technology, 3200003, Haifa, Israel and

³ Centre for Quantum Technologies, National University of Singapore, 117543 Singapore, Singapore

We present a new framework for a scalable benchmarking of a quantum computer that is based on local expectation values, measured on the steady state of an engineered, non-unital and dissipative channel. Such channels can be efficiently implemented on the quantum computer using mid-circuit measurements or RESET gates. We show that the expectation values of local Pauli operators in that state satisfy a set of local constraints that (i) depend on the underlying channel parameters, and (ii) can be checked efficiently. This gives us a simple way to check how well a given noise model describes the actual hardware when all qubits are being actively used for non-negligible amount of time. Moreover, as we do not need to classically calculate these expectation values, our method evaluates a quantum computer in a regime that might be classically inaccessible. Finally, given a parameterized noise model, we can use our method to learn the underlying noise parameters for the entire system. We demonstrate our method numerically and experimentally on an IBMQ machine, and show that a full noise model can be verified and learned from Pauli measurements on a single circuit output.

I. INTRODUCTION

In recent years, with the advances in quantum information and quantum computation, there have been a growing interest in methods for learning many-body quantum systems. These methods include, for example, recovering a many-body Hamiltonian based on its dynamics [1–11], its steady states [12–15], or using a trusted quantum simulator [16–20].

Among these methods, a promising line of research tries to learn the underlying generators of dynamics using local measurements on a steady state of the system [21– 27. It can be shown that if the underlying Hamiltonians or Lindbladians are sufficiently generic, they can be uniquely determined by the expectation values of local observables in such steady states. Specifically, Ref. [25] shows that there exist a set of *local* linear constraints between expectation values of local Paulies in a steady state of the system. If we measure these expectation values in a given patch of the system, we can infer the underlying Hamiltonian or Lindbladian terms in that region [28]. In some respect, at least in the case of local Hamiltonians, the method relies on the non-commutativity of the local Hamiltonian terms, and is therefore a 'purely quantum' method, with no classical equivalent. It gives a surprisingly simple and efficient method for learning the generators of the local dynamics, and can also be used to test how well a particular model of the Hamiltonian or Lindbladian agrees with the empirical measurements. All this is done without having to classically calculate these expectation values, which is crucial for the scalablity of the approach.

The simplicity and efficiency of the above methods raises the question of whether and how they can be applied to quantum computers. Can we define "steady-states" of quantum computers? Can we find constraints on local expectation values in these states that can be used to benchmark the quantum computer or even learn a (noisy) gate set?

A quantum computer has several key distinctions from local Hamiltonians and Lindbladians. The latter evolve continuously, whereas, at least in an abstract level, a quantum computer evolves in a discrete, gate-based fashion. In addition, the steady state of a unitary circuit is any convex combination of its eigenstates, and it is not clear how to prepare them efficiently. Moreover, the presence of noise changes this picture significantly by breaking unitarity and the purity of the underlying quantum states.

In this work we propose a method that overcomes these obstacles and generalizes the approach of Ref. [25] to the realm of gate-based quantum computers. Our main idea is to engineer a dissipative channel that can be implemented on a quantum computer using non-unitary gates such as the RESET gates. By iteratively applying this channel, we rapidly reach a fixed point, on which we can measure local expectation values. These expectation values satisfy an extensive set of local linear constraints among themselves, which can be efficiently tested without having to classically estimate these expectation values. Therefore, they can be used to benchmark how well a noise model describes the underlying quantum computer. They can also be leveraged to learn such model from a parameterized set of models using a variational technique.

Engineered dissipative steady-states are becoming an increasingly useful part of the NISQ-era toolbox due to their ability to naturally incorporate or even take advantage of unavoidable noise effects [29–36]. Our method suggests that they can also hold a finger print of the underlying noise in the system, and therefore

^{*} yigal.ilin@gmail.com

used for benchmarking and characterization. More importantly, as shown in Ref. [37], engineered dissipative steady-states can encode universal quantum computations. Therefore by measuring dissipative steady states, we are evaluating a quantum computer in a regime that may be classically inaccessible. Additionally, the steady states that we measure can be the result of actively using all qubits in the system simultaneously, and therefore our method can give a global picture of the noise in the system. Finally, since we are only measuring the steady state, our method is insensitive to state preparation errors, and is also not limited by the qubits decoherence time.

Like the methods of Refs. [24–27], our method is highly scalable, and can be used on systems with a large number of qubits. To demonstrate it, we introduce two possible dissipative maps. The first map is a stochastic map, which can be described as a local Kraus map (at least in the absence of noise). It can be implemented on a quantum computer by randomly applying a gate from a set of gates with a prescribed set of probabilities. Consequently, the steady state is probed by running many different random circuits, which realize different trajectories of the dynamics. The second map is a deterministic map that is based on a composed 2-local gate, which is both non-unitary and entangling. Implementing this map on a quantum computer requires only one circuit. which makes it easier to execute on currently available hardware such as IBMQ. To test our method we used numerical simulations of both maps on 5–11 gubits, and in addition applied the deterministic map to an IBMQ machine using 5 qubits.

We note that as a noise characterization tool, our method cannot match the precision of established methods such as randomized benchmarking (RB) [38–41], or gate-set tomography (GST) [42–44]. This is mainly due to the fact that these methods utilize a form of "error amplification", where different components of the quantum channel can be measured with accuracy O(1/M) using only M shots. In comparison, our method relies on the accuracy of the local expectation values that scales as $O(1/\sqrt{M})$. This imposes a higher upper bound on the overall accuracy of the characterization, approximately scaling as $O(1/\sqrt{M})$. Nevertheless, in contrast to RB, it can be used to learn the direct noise channel instead of an average, twirlled version of it. Also, in contrast with GST, it can benchmark the noise *globally* when all qubits are being actively used, thereby giving a holistic picture of the noise in the system.

The structure of this paper is as follows. In Sec. II we provide brief definitions and basic facts on quantum channels and gates, and the notation we use throughout the paper. Then in Sec. III we introduce the theoretical framework of learning a local quantum channel from its steady state, and how this can be implemented on a quantum computer. In Sec. IV we define the noise model we will be using to characterize and benchmark the IBMQ machines. We also briefly describe the opti-

mization method used in the variational learning part. In Sec. V we describe the results of our numerical simulations, performed on the two types of engineered dissipative dynamics. In Sec. VI we present the results of applying our method on an actual IBMQ machine using 5 qubits, which include benchmarking different noise models, as well as using our method to learn its noise. Finally, in Sec. VII we present our conclusions and discuss possible future research directions.

II. PRELIMINARIES

Throughout this work we consider a quantum computer (QC) made of n qubits with Hilbert space $(\mathbb{C}^2)^{\otimes n}$. Quantum states will be generally denoted by Greek letters ρ , σ , etc. The expectation value of an observable A with respect to the quantum state ρ will be generally denoted by $\langle A \rangle_{\rho} = \text{Tr}(\rho A)$.

Unitary gates will be denoted by X, Y, Z, CX, R_x , etc. We use $CX(i \rightarrow j)$ to denote the CNOT (Controlled-NOT) gate between the control qubit i and the target qubit j. We use $R_x(\theta)$ to denote a Bloch sphere rotation of angle θ around the axis x. Quantum channels, i.e., completely positive, trace-preserving (CPTP) maps will usually be denoted by calligraphic letters such as $\mathcal{E}(\cdot), \mathcal{N}(\cdot)$, etc. Given a unitary gate U, we will denote its corresponding channel by \mathcal{U} , i.e., $\mathcal{U}(\rho) \stackrel{\text{def}}{=} U \rho U^{\dagger}$. For any quantum channel \mathcal{E} , its adjoint is the unique superoperator \mathcal{E}^* that satisfies $(\mathcal{E}^*(A), B) = (A, \mathcal{E}(B))$ for any operators A, B, where $(A, B) \stackrel{\text{def}}{=} \operatorname{Tr}(A^{\dagger}B)$ is the Hilbert-Schmidt inner product between two operators. A map \mathcal{E} is trace preserving if and only if $\mathcal{E}^*(\mathbb{I}) = \mathbb{I}$. A channel $\mathcal{E}(\cdot)$ is called *unital* if it also holds that $\mathcal{E}(\mathbb{I}) = \mathbb{I}$. In other words, the maximally mixed state is a fixed point of the channel.

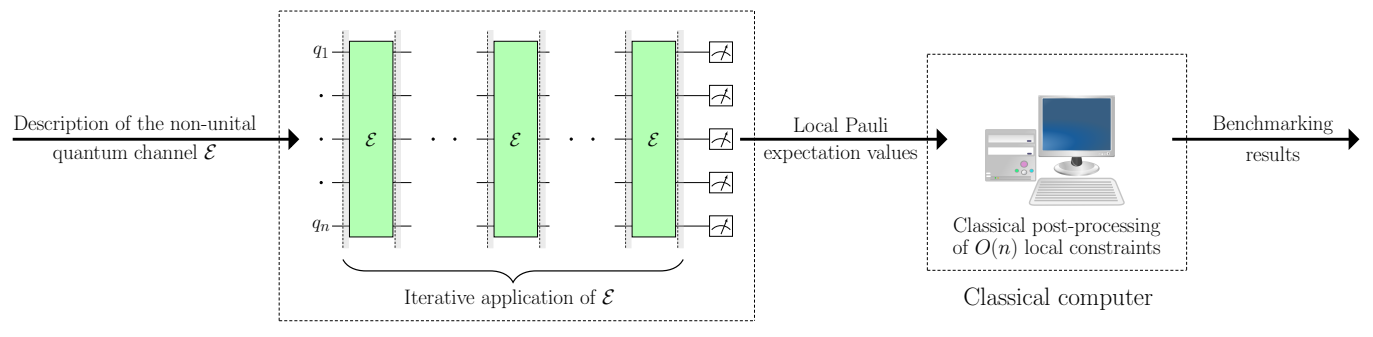
An important example of a non-unital channel that can be applied on a QC is formed by the RESET gate, which performs an active, mid-circuit reset of a qubit to the $|0\rangle$ state. Ideally, it corresponds to the channel

$$\mathcal{E}_{\text{RESET}}(\rho) = |0\rangle\langle 1|\rho|1\rangle\langle 0| + |0\rangle\langle 0|\rho|0\rangle\langle 0|.$$

It can also be realized by measuring the qubit in the standard basis, and applying X gate whenever the result is $|1\rangle$.

III. LEARNING QUANTUM CHANNELS FROM THEIR STEADY STATE

In this section we introduce our method for verifying and learning quantum channels using local measurements on their steady state. Since our goal is to apply this method to quantum computers, we shall consider channels that can be implemented on a quantum computer. We briefly summarize the main steps of our method in Fig. 1 as a block-diagram.



Quantum computer with n qubits

FIG. 1. Block diagram summarizing our method. Given a description of the non-unital channel $\mathcal{E}(\cdot)$ (e.g. its quantum gates, activation probabilities, etc), we iteratively apply it on a QC to reach an approximate steady state. The local Pauli expectation values are sampled from the steady state, and used as input to the classical post-processing routine. They satisfy a set of local constraints with coefficients that depend on the noise parameters of the underlying quantum device. The local constraints can be verified efficiently and their number grows linearly with the system size. To *validate* a given noise model, we use these constraints to define a *cost function* that measures how much they are violated, and check how close it is to zero. To *learn* a noise model, we use an optimization routine to minimize the cost function over a set of possible noise models.

Let us then denote by $\mathcal{E}(\cdot)$ such a quantum channel. Two examples to keep in mind are (i) the application of quantum gate drawn from a set of gates according to a fixed probability distribution, and (ii) a low-depth quantum circuit. In both examples, we assume that the overall channel is non-unital because of the noise and/or because of actively using the RESET gate. Unlike unital channels, whose fixed point is typically the maximally mixed state, the fixed points of non-unital channels are typically non-trivial in the sense that two different channels from a relevant set of channels will have different fixed points. We shall further assume that $\mathcal{E}(\cdot)$ has a unique fixed point $\mathcal{E}(\rho_{\infty}) = \rho_{\infty}$, which we call the steady state. We shall also assume that ρ_{∞} can be approximately reached by the QC using few applications of \mathcal{E} , starting from an initial state $\rho_0 = |0\rangle\langle 0|^{\otimes n}$. For brevity, we will denote expectation values with respect to ρ_{∞} by $\begin{array}{l} \langle \cdot \rangle_{\infty} \text{ instead of } \langle \cdot \rangle_{\rho_{\infty}}. \\ \text{Given a channel } \mathcal{E}, \text{ assume that the system is in its} \end{array}$

Given a channel \mathcal{E} , assume that the system is in its steady state ρ_{∞} . Then the expectation value of any observable A must satisfy

$$\langle A \rangle_{\infty} = \text{Tr}(A\rho_{\infty}) = \text{Tr}(\mathcal{E}^*(A)\rho_{\infty}) = \langle \mathcal{E}^*(A) \rangle_{\infty}.$$
 (1)

The above equation is the basis of our method. For the channels that will be discussed below, when A is a local observable, the observable $\mathcal{E}^*(A)$ is also local, or at least can be estimated using local measurements. In such case, we can use the equality between the LHS and RHS to constrain, or even learn \mathcal{E} , without having to calculate the expectation values in ρ_{∞} — which is in general exponentially expensive in n. Moreover, as we are measuring the steady state of the system, our results are independent from the initial state of the system, and therefore insensitive to state preparation errors.

Below, we describe two methods to construct such \mathcal{E} . In Sec. III A and Sec. III B we describe a stochastic method of creating \mathcal{E} , and in Sec. III C describe a

deterministic method.

A. A stochastic map: the strictly local case

Let $\{\mathcal{E}_k\}$ be a set of local channels implementable by a QC. We can think of every \mathcal{E}_k as being the application of a quantum gate or of several gates acting on a small contiguous subset of qubits. In practice, we will always use \mathcal{E}_k that act on at most two neighboring qubits. In addition, we will allow some of the \mathcal{E}_k to be non-unital by containing RESET gates. Together with $\{\mathcal{E}_k\}$, we will use a probability distribution $\{p_k\}$ and define our quantum channel by

$$\mathcal{E} \stackrel{\text{def}}{=} \sum_{k} p_k \mathcal{E}_k. \tag{2}$$

Physically, \mathcal{E} can be implemented on a QC in a stochastic way: we choose a k with probability p_k and apply \mathcal{E}_k .

For example, the three qubits non-unital quantum channel

$$\mathcal{E}(\rho) = 0.2 \cdot X_1^{1/2} \rho X_1^{1/2^{\dagger}} + 0.2 \cdot \text{CX}(1 \to 2) \rho \, \text{CX}(1 \to 2) + 0.4 \cdot \text{CX}(2 \to 3) \rho \, \text{CX}(2 \to 3) + 0.2 \cdot \text{RESET}_3(\rho)$$

can be implemented on a QC by randomly applying one of the gates $\{X_1^{1/2}, \mathrm{CX}(1\to 2), \mathrm{CX}(2\to 3), \mathrm{RESET}_3\}$ according to the probabilities $\{0.2, 0.2, 0.4, 0.2\}$. A simple numerical check shows that the steady state of the this channel is a non-product state which can be approximated to within a trace distance of 10^{-5} using few tens of steps.

Plugging Eq. (2) in Eq. (1), we see that for any local

observable A,

$$\langle A \rangle_{\infty} = \sum_{k} p_k \langle \mathcal{E}_k^*(A) \rangle_{\infty}.$$
 (3)

Importantly, if \mathcal{E}_k is a 2-local channel, then \mathcal{E}_k^* also acts non-trivially only on the two-qubits on which \mathcal{E}_k is defined. Consequently, if A is a t-local observable, then $\mathcal{E}_k^*(A)$ is at most a (t+2)-local observable. In fact, it is at most (t+1) for the following reason. The only case where $\mathcal{E}_k^*(A)$ might be (t+2)-local is when the supports of \mathcal{E}_k and A are disjoint. But in such case, $\mathcal{E}_k^*(A) = A\mathcal{E}_k^*(\mathbb{I}) = A$, which is t-local.

Using this observation, we may write Eq. (3) as

$$\langle A \rangle_{\infty} = \sum_{k \in \text{supp}(A)} p_k \langle \mathcal{E}_k^*(A) \rangle_{\infty} + \sum_{k \notin \text{supp}(A)} p_k \langle A \rangle_{\infty},$$

where we use the notation $k \in \operatorname{supp}(A)$ to denote enumeration over all k indices for which \mathcal{E}_k acts non trivially on A. Writing the LHS as $\sum_{k \in \operatorname{supp}(A)} p_k \langle A \rangle_{\infty} + \sum_{k \notin \operatorname{supp}(A)} p_k \langle A \rangle_{\infty}$ and re-organizing the equation, we obtain the following equation, which holds for every local observable A:

$$\sum_{k \in \text{supp}(A)} p_k \left(\langle \mathcal{E}_k^*(A) \rangle_{\infty} - \langle A \rangle_{\infty} \right) = 0.$$
 (4)

The above equation can be used to validate a given model of the local channels $\{\mathcal{E}_k\}$. Indeed, given a model for the local channels, together with a corresponding probability distribution $\{p_k\}$, we define a cost function Φ by taking the square of the difference between the LHS and RHS of Eq. (4) for a set of independent local observables $\{A\}$:

$$\Phi \stackrel{\text{def}}{=} \sum_{A} \left(\sum_{k \in \text{supp}(A)} p_k \left(\langle \mathcal{E}_k^*(A) \rangle_{\infty} - \langle A \rangle_{\infty} \right) \right)^2.$$
 (5)

Since $\langle \mathcal{E}_k^*(A) \rangle_{\infty}$ is the expectation value of a (t+1)-local observable, we can express it as a linear combination of the expectation value of (t+1)-local Pauli strings on the same support. The resulting Φ can then be written as a quadratic expression of these Pauli expectation values, with coefficients $C_{\alpha\beta}$ that depend on the details of underlying model:

$$\Phi = \sum_{A} \sum_{\alpha,\beta} C_{\alpha\beta}^{(A)} \langle P_{\alpha} \rangle_{\infty} \langle P_{\beta} \rangle_{\infty}.$$
 (6)

Therefore, by measuring the (t+1)-local Pauli expectation values in the steady state, we can calculate Φ and see how well the model fits the actual quantum hardware.

This procedure can also be made local by considering local cost functions Φ_q for qubit q. Denoting by I_q the set of observables A for which $\mathcal{E}_k^*(A)$ acts non-trivially on q, the local cost function is given by

$$\Phi_q \stackrel{\text{def}}{=} \frac{1}{|I_q|} \sum_{A \in I_q} \left(\sum_{k \in \text{supp}(A)} p_k \langle \mathcal{E}_k^*(A) \rangle_{\infty} - \langle A \rangle_{\infty} \right)^2, \quad (7)$$

where the $|I_q|$ is the number of elements in I_q . In general, $|I_q|$ can be different for different qubits, e.q., for qubits arranged on a line the boundary qubits on each end of the system will have a smaller $|I_q|$.

The local validation scheme allows us to identify the regions in the system where the model performs well or badly in a setup in which possibly all the device qubits are being actively used. Because it only requires (t+1)-local expectation values, it is highly scalable and has a small computational cost.

The above idea can be pushed further; we can actually use Eq. (4) to *learn* the local \mathcal{E}_k channels. Suppose we have some parameterization of \mathcal{E}_k , denoted by $\mathcal{E}_{k,\theta}$, where θ is a vector of parameters. We may define the θ -dependent cost function

$$\Phi(\boldsymbol{\theta}) \stackrel{\text{def}}{=} \sum_{A} \left(\sum_{k \in \text{supp}(A)} p_k \left(\left\langle \mathcal{E}_{k,\boldsymbol{\theta}}^*(A) \right\rangle_{\infty} - \left\langle A \right\rangle_{\infty} \right) \right)^2,$$
(8)

and find the particular $\boldsymbol{\theta}$ that best describes the system by $minimizing~\Phi(\boldsymbol{\theta})$. As before, we can write $\Phi(\boldsymbol{\theta})$ as a quadratic expression of the expectation values of (t+1)-local Paulis in the steady state with $\boldsymbol{\theta}$ -dependent coefficients:

$$\Phi(\boldsymbol{\theta}) = \sum_{A} \sum_{\alpha\beta} C_{\alpha\beta}^{(A)}(\boldsymbol{\theta}) \langle P_{\alpha} \rangle_{\infty} \langle P_{\beta} \rangle_{\infty}. \tag{9}$$

Estimating these local Pauli expectations at the steady state allows us to learn the best θ that describes the quantum hardware.

The θ parameterization can be full, in which case we would need about 16×16 parameters to describe all possible 2-qubit channels \mathcal{E}_k , or it could contain a much smaller number of parameters if we use prior assumptions on the structure of \mathcal{E}_k .

For a system with n qubits, there are exactly $N_t = \sum_{k=1}^t 3^k (n-k+1)$ t-local Pauli operators with contiguous support, not counting the trivial identity operator. By selecting t-local Pauli operators as the observables A in Eq. (8), we effectively minimize over N_t constraints, and therefore it is desirable that the number of free parameters will be smaller than N_t . For example, we may model the channel that corresponds to an $R_x(\alpha)$ rotation using one parameter — α , in order to see if the hardware gate under-rotates or over-rotates with respect to the \hat{x} axis.

B. A stochastic map: the non strictly-local case

In the previous section we derived our main equation, Eq. (4), under the assumption that \mathcal{E}_k are strictly local channels, acting non trivially on at most O(1) qubits. This is assumption is longer true in realistic noise models, in which also idle qubits, far away from the support of \mathcal{E}_k , experience noise such as dephasing and amplitude

damping. In this section we show how our method can be generalized to account also for such cases. Specifically, we shall assume a local Markovian noise model without cross talks, with the following properties:

- Each qubit j has its own idle noise channel N_j, which acts independently of what happens to the other qubits. Thus the noise on the set of idle qubits I_{idle} factors into a tensor product of single-qubit noise channels ⊗_{j∈I_{idle}} N_j.
- 2. When a unitary gate or a RESET gate acts on one or two qubits, the actual channel applied by the QC is a noisy version of these gates that acts only on the qubits in the support of the ideal gates (i.e., no spillover or cross-talks to other qubits), together with the idle noise channel on the rest of the qubits.

Together, these two assumptions imply that every local channel \mathcal{E}_k in the strictly local case is replaced by the non-local channel $\tilde{\mathcal{E}}_k \otimes \bigotimes_{j \notin \text{supp}(k)} \mathcal{N}_j$, where $\tilde{\mathcal{E}}_k$ is the noisy version of \mathcal{E}_k and supp(k) denotes the qubits in the support of \mathcal{E}_k (which, under our assumptions, also define the support of $\tilde{\mathcal{E}}_k$).

To proceed, we define superoperators \mathcal{F}_k

$$\mathcal{F}_k \stackrel{\text{def}}{=} \left(\bigotimes_{j \in \text{supp}(k)} \mathcal{N}_j^{-1} \right) \tilde{\mathcal{E}}_k. \tag{10}$$

We will use \mathcal{F}_k as a mathematical tool to simplify the equations we derive below. Note that \mathcal{F}_k is not necessarily a channel, since \mathcal{N}_j^{-1} by itself is not necessarily a channel. Nevertheless it is a *local* superoperator which satisfies $\mathcal{F}_k(A) = A$ when A is outside its support. The point of using \mathcal{F}_k is that it allows us to write the global action of the kth local channel without the $j \notin \text{supp}(k)$

condition:

$$\tilde{\mathcal{E}}_k \otimes \bigotimes_{j \notin \operatorname{supp}(k)} \mathcal{N}_j = \left(\bigotimes_j \mathcal{N}_j\right) \cdot \mathcal{F}_k.$$

Plugging this expression to Eq. (1), we obtain the non strictly-local version of Eq. (3):

$$\langle A \rangle_{\infty} = \sum_{k} p_{k} \langle (\mathcal{F}_{k}^{*} \cdot \bigotimes_{i} \mathcal{N}_{i}^{*}) A \rangle_{\infty}.$$
 (11)

By the same argument used in the previous section, we note that the local noise channels act on A non-trivially only if they are in its support, and therefore we can define a "noisy version" of A by

$$\left(\bigotimes_{j} \mathcal{N}_{j}^{*}\right)(A) = \left(\bigotimes_{j \in \text{supp}(k)} \mathcal{N}_{j}^{*}\right)(A) \stackrel{\text{def}}{=} \tilde{A}.$$

Plugging this back into Eq. (11), we get the equation

$$\langle A \rangle_{\infty} = \sum_{k} p_{k} \langle \mathcal{F}_{k}^{*}(\tilde{A}) \rangle_{\infty}.$$
 (12)

This equation is almost identical to its strictly-local counterpart Eq. (3), except that in the RHS A is replaced by \tilde{A} and \mathcal{E}_k^* is replaced by \mathcal{F}_k^* . Following the same logic as in the previous case, we use the fact that as \mathcal{F}_k is local, $\langle F_k^*(A)\rangle_{\infty} = \langle A\rangle_{\infty}$ whenever A is outside its support. Therefore, subtracting $\langle \tilde{A}\rangle_{\infty}$ from both sides, we obtain the final equation in which the summation in the RHS is only over channels that intersect with A:

$$\langle A - \tilde{A} \rangle_{\infty} = \sum_{k \in \text{supp}(A)} p_k \left(\langle \mathcal{F}_k^* (\tilde{A}) \rangle_{\infty} - \langle \tilde{A} \rangle_{\infty} \right).$$
 (13)

As in the previous section, we can use the above set of constraints as a validation tool for particular noise models by defining local cost functions, as done in Eq. (7). We can also use it to learn the best noise model from a family of noise models parameterized by θ , by using the global cost function

$$\Phi(\boldsymbol{\theta}) \stackrel{\text{def}}{=} \sum_{A} \left(\sum_{k \in \text{supp}(A)} p_k \left(\langle \mathcal{F}_{k,\boldsymbol{\theta}}^* (\tilde{A}_{\boldsymbol{\theta}}) \rangle_{\infty} - \langle \tilde{A}_{\boldsymbol{\theta}} \rangle_{\infty} \right) - \langle A - \tilde{A}_{\boldsymbol{\theta}} \rangle_{\infty} \right)^2.$$
 (14)

As before, to evaluate $\Phi(\boldsymbol{\theta})$ from local measurements, we expand the operators $\tilde{A}_{\boldsymbol{\theta}}$, $\mathcal{F}_{k,\boldsymbol{\theta}}^*(\tilde{A}_{\boldsymbol{\theta}})$ in terms of (t+1)-local Pauli strings with $\boldsymbol{\theta}$ -dependent coefficients and write the cost function $\Phi(\boldsymbol{\theta})$ is a quadratic expression of these expectations (see Eq. (9)).

C. Deterministic map

Realizing the method presented in the previous Sec. III B on a QC requires the execution of a large number of different quantum circuits, or trajectories, in order to properly sample the steady state. This makes it challenging to implement on currently available devices, which are often limited by the number of distinct circuits

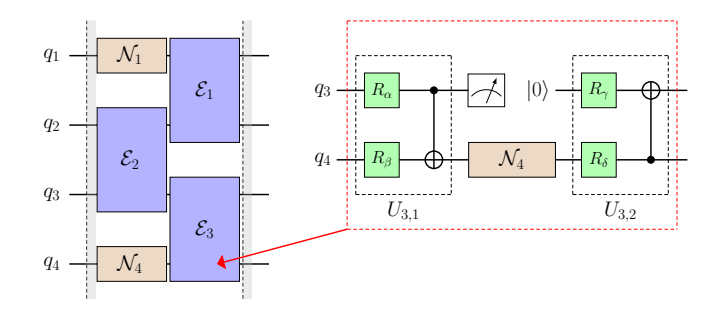


FIG. 2. Example of the deterministic channel implementation on a QC. Left: Odd channel \mathcal{E}_I applied on four qubits, the even layer $\mathcal{E}_{\text{even}}$ is followed by the odd layer \mathcal{E}_{odd} . During the action of the \mathcal{E}_2 on qubits 2,3 in the even layer, we assume that the idle noise channels $\mathcal{N}_1, \mathcal{N}_4$ are acting on the qubits 1,4. Right: Inner structure of the 2-local channel \mathcal{E}_3 . The 2-local non-unital channel \mathcal{E}_3 consists of applying a two-qubit unitary gate $U_{3,1}$ on qubits 3,4, followed by a RESET gate on qubit 3 along with idle noise channel \mathcal{N}_4 on qubit 4, and ends with applying a two-qubit unitary gate $U_{3,2}$. The two-qubit unitary gate $U_{3,1}$ has two known single-qubit rotation gates R_{α} , R_{β} about axes $\hat{\alpha}$ and $\hat{\beta}$ together with a CX gate. The exact details of our realization of the noisy non-unital channels $\{\mathcal{E}_k\}$ are given in Sec. V C 1.

that can be executed in a single experimental batch.

To overcome this limitation, we propose an alternative way to construct a non-unital channel, which relies on a deterministic map that can be implemented on a QC using a single circuit. For simplicity, we shall describe our construction in the 1D case with open boundary conditions, but generalization to other geometries and higher dimensions is straightforward. In such case, our map \mathcal{E} is defined by a product of local channels $\{\mathcal{E}_k\}$, where \mathcal{E}_k acts non-trivially on the neighboring qubits k, k+1. The \mathcal{E}_k channels are organized in a two layers brick-wall structure, as shown in Fig. 2.

As explained in Sec. III, to learn the parameters of the quantum channel, we want its steady state to be non-trivial in the sense that it will not be the steady state of other local channels. To that aim, we want the local \mathcal{E}_k channels to be non-unital and also entangling so that the steady state will be a non trivially-entangled state. For example, such \mathcal{E}_k may be realized on a QC by some combination of CX, single-qubit rotations, and RESET gates, as shown in Fig. 2 and discussed below.

To derive our constraints, we view \mathcal{E} as the product of two layers. We define the *odd layer* by $\mathcal{E}_{\mathrm{odd}} \stackrel{\mathrm{def}}{=} \bigotimes_{\mathrm{odd} k} \mathcal{E}_k$ and even layer by $\mathcal{E}_{\mathrm{even}} \stackrel{\mathrm{def}}{=} \bigotimes_{\mathrm{even} k} \mathcal{E}_k$. There are two possible choices for the overall channel \mathcal{E} , based on the order in which the layers are applied: $\mathcal{E}_I \stackrel{\mathrm{def}}{=} \mathcal{E}_{\mathrm{odd}} \cdot \mathcal{E}_{\mathrm{even}}$ and $\mathcal{E}_{II} \stackrel{\mathrm{def}}{=} \mathcal{E}_{\mathrm{even}} \cdot \mathcal{E}_{\mathrm{odd}}$. An example of the \mathcal{E}_I channel is given in Fig. 2. The steady state of \mathcal{E}_{II} is defined by $\mathcal{E}_I(\rho_\infty^I) = \rho_\infty^I$, and the steady state of \mathcal{E}_{II} by $\mathcal{E}_{II}(\rho_\infty^{II}) = \rho_\infty^{II}$. In general, they will differ from each other. For brevity, expectation values calculated under ρ_∞^I , ρ_∞^{II} are denoted by $\langle \cdot \rangle_I$, $\langle \cdot \rangle_{II}$ respectively.

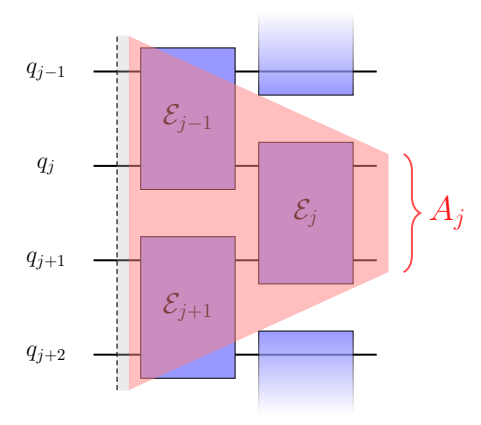


FIG. 3. A light cone originating from a 2-local observable A_j (red shaded area) has at most 4-local support. For the case of finite system with open boundary conditions the light cone is truncated from 4-local to 3-local at each end of the system.

Let us now apply Eq. (1) to the case of \mathcal{E}_I and a local observable A:

$$\langle A \rangle_I = \langle \mathcal{E}_I^*(A) \rangle_I = \langle \mathcal{E}_{\text{even}}^* (\mathcal{E}_{\text{odd}}^*(A)) \rangle_I.$$
 (15)

To simplify the equation, we restrict our attention to observables A_j acting on qubits j, j+1 for odd j. The support A_j coincides with the support of \mathcal{E}_j from \mathcal{E}_{odd} . By the same argument that was used in Sec. III A, if the supports of \mathcal{E}_k and A_j are disjoint, $\mathcal{E}_k^*(A_j) = A_j$, and so $\mathcal{E}_{\text{odd}}^*(A_j) = \mathcal{E}_j^*(A_j)$. Another simplification comes from the fact that the light cone of A_j has support only on \mathcal{E}_{j-1}^* and \mathcal{E}_{j+1}^* , as shown in Fig. 3. Therefore, $\mathcal{E}_{\text{even}}^*(\mathcal{E}_{\text{odd}}^*(A_j)) = (\mathcal{E}_{j-1}^* \otimes \mathcal{E}_{j+1}^*)(\mathcal{E}_j^*(A_j))$. All together, this allows us to rewrite Eq. (15) in terms of 4-local expectation values on the RHS:

$$\langle A_j \rangle_I = \langle (\mathcal{E}_{j-1}^* \otimes \mathcal{E}_{j+1}^*) \mathcal{E}_j^* (A_j) \rangle_I.$$
 (16)

For observables A_j with even j, a similar equation holds with the steady state of \mathcal{E}_{II} replacing the steady state of \mathcal{E}_I .

Following our previous construction with the stochastic map, we can use the constraints in Eq. (16) to validate a given model for the local channels, or learn the model that best fits the data from a family of models characterized by a set of parameters θ . For the learning task, we start by defining the cost function $\Phi_I(\theta)$ using expectation values in the steady state ρ_{∞}^I :

$$\Phi_{I}(\boldsymbol{\theta}) \stackrel{\text{def}}{=} \sum_{A_{j}} \left(\left\langle \left[\mathcal{E}_{j-1,\boldsymbol{\theta}}^{*} \otimes \mathcal{E}_{j+1,\boldsymbol{\theta}}^{*} \right] \mathcal{E}_{j,\boldsymbol{\theta}}^{*}(A_{j}) \right\rangle_{I} - \left\langle A_{j} \right\rangle_{I} \right)^{2}.$$
(17)

Above, the sum is over a set of 2-local observables A_j defined on j, j+1 for odd j, which we take to be Pauli operators. Similarly, we define $\Phi_{II}(\boldsymbol{\theta})$ from the expectation values at ρ_{∞}^{II} , and set

$$\Phi(\boldsymbol{\theta}) \stackrel{\text{def}}{=} \Phi_I(\boldsymbol{\theta}) + \Phi_{II}(\boldsymbol{\theta}). \tag{18}$$

For a system with n qubits, there are exactly 3n+9(n-1)=12n-9 such geometrically 2-local Pauli operators, excluding the trivial identity operator. This number provides a rough upper bound to the number of parameters that can be learned using this method.

To validate a given model, we define local cost functions Φ_q , which for a given q contain all terms in Φ_I , Φ_{II} that overlap q. See Eq. (7) for the equivalent definition in the stochastic case.

As in the case of the stochastic map, we can expand $\mathcal{E}_{I}^{*}(A), \mathcal{E}_{II}^{*}(A)$ in terms of 4-local Pauli operators, and write $\Phi(\theta)$ as a quadratic expression of the expectation values of these operators, as done in Eq. (9).

There are many ways to realize the non-unital channels \mathcal{E}_k on a QC. In this work we use a composed gate, which we call the RESU gate (RESU = RESET + unitary). It is defined by two 2-local unitaries $U_{k,1}$ and $U_{k,2}$ acting on qubits k, k+1 and a RESET gate on qubit k. Each of the 2-local unitaries is made of a CNOT and two general 1-qubit rotations, as shown in Fig. 2. Further details of how we model this gate in the presence of noise are given in Sec. V C 1.

In Sec. VC we show numerically that our protocol can be used to learn a given noise model, and in Sec. VI we demonstrate its performance on actual quantum hardware.

IV. NOISE MODELS AND CLASSICAL OPTIMIZATION

In this section we describe the noise models and the numerical procedures we used to find θ by optimizing over the cost functions in Eqs. (14, 18),

A. Local Markovian noise models

We assume a local Markovian noise model, which can be generally treated using the Lindbladian master equation [45–47]. To model the evolution of a noisy quantum gate, we write

$$\frac{d}{dt}\rho = -\frac{i}{T_0}[H_k(\boldsymbol{\theta}_k), \rho] + \frac{1}{T_0} \sum_m \theta_m \mathcal{L}_m(\rho).$$
 (19)

Above, T_0 is a time scale, to be determined later, and the dimensionless Hamiltonian $H_k(\boldsymbol{\theta}_k)$ defines the coherent evolution of the gate U_k , i.e., $U_k = e^{-iH_k(\boldsymbol{\theta}_k)T/T_0}$, where T is the gate time and $\{\boldsymbol{\theta}_k\}$ are variational gate parameters. For example, the $\{\boldsymbol{\theta}_k\}$ parameters may describe a source of coherent error in the two-qubit CX gate.

Under our local noise assumption, we take \mathcal{L}_m to be single-qubit superoperators that represent different single-qubit noise processes. They are given in terms of jump operators L_m , $\mathcal{L}_m(\rho) \stackrel{\text{def}}{=} L_m \rho L_m^{\dagger} - \frac{1}{2} \{L_m^{\dagger} L_m, \rho\}$, where $\{\cdot, \cdot\}$ is an anti-commutator. The variational parameters $\{\theta_m\}$ model the strength of the different noise

processes. For example, for a single-qubit dephasing noise, we use $\mathcal{L}_z(\rho) = Z\rho Z - \rho$, and the corresponding θ/T_0 is the decoherence rate.

Given a set of channels $\{\mathcal{E}_k\}$ that define either the stochastic or the deterministic maps, we take T_0 to be the maximum over the running times of $\{\mathcal{E}_k\}$. Working with the IBMQ hardware, this time scale was primarily due to the RESET gate time, which is typically on the order of a microsecond [48, 49]. The T_0 and gate execution times we used in our numerical simulations are given in Appendix B and Appendix C.

We allowed the coupling strength (variational) parameters to be different for each qubit. For a qubit j, we use the notation $\boldsymbol{\theta}^{(j)} = \{\theta_m^{(j)}\}$ to denote its relevant noise parameters.

Using the above assumptions, the noise channel $\mathcal{N}_{\boldsymbol{\theta}^{(j)}}$ on an idle qubit j for time T is represented by:

$$\mathcal{N}_{\boldsymbol{\theta}^{(j)}}(\rho) = e^{\frac{T}{T_0} \sum_m \theta_m^{(j)} \mathcal{L}_m}(\rho). \tag{20}$$

Similarly, the noisy version of a unitary gate U_k described by a Hamiltonian $H_k(\theta)$ acting for time T is given by:

$$\tilde{\mathcal{E}}_{k \; \boldsymbol{\theta}^{(j)}}(\rho) = e^{\frac{T}{T_0} \left(-i[H_k(\boldsymbol{\theta}_k), \cdot] + \sum_m \theta_m^{(j)} \mathcal{L}_m\right)}(\rho). \tag{21}$$

If U_k is a two-qubits gate, the above equation will contain the $\theta_m \mathcal{L}_m$ operators of both qubits.

Equation (21) in its entirety was in fact only used to model the noisy CX gate when analyzing the experimental data from the IBMQ hardware. For the single qubit gates, or for the CX gate in the numerical simulations, no coherent errors were assumed, and $H_k(\theta_k)$ was taken to be the ideal Hamiltonian, which is independent of θ_k . The full details of the CX modeling we used are given in Appendix A.

Another simplification was the use of a first-order Trotter-Suzuki approximation for the case of single-qubit gates. As the typical execution time of these gates is much shorter than that of the CX gate (in the IBMQ hardware their execution time is the range of tens of nanoseconds [48, 49], which is about an order of magnitude shorter than the execution time of CX), we approximated Eq. (21) by

$$\tilde{\mathcal{E}}_{k,\boldsymbol{\theta}^{(j)}} \simeq \mathcal{U}_k \cdot \mathcal{N}_{\boldsymbol{\theta}^{(j)}}.$$
 (22)

Above, $\mathcal{U}_k(\cdot) \stackrel{\text{def}}{=} e^{-i\frac{T}{T_0}[H_k,\cdot]}$ is the ideal single-qubit gate channel. Notice that as the resultant error of this approximation scales as $O\left((T/T_0)^2 \cdot \|[[H_k,\cdot],\sum_m \theta_m^{(j)}\mathcal{L}_m]\|\right)$, and as $\|H_k\|$ and $\|\theta_m\mathcal{L}_m\|$ are all O(1) (see Appendix B and Appendix C for more details), we deduce that our Trotter-Suzuki error for single-qubit gates is of the order of $\left(T/T_0\right)^2 \sim 10^{-4}$, which is much smaller than all other error sources (e.g., statistical error) described below.

We conclude this section by describing how we modeled the noisy RESET gate. Here we followed Ref. [32] and modeled the noisy gate phenomenologically using a Kraus map representation. In this approach, the noisy RESET gate on the qubit j is described by two variational parameters, $\boldsymbol{\theta}^{(j)} = (\theta_0^{(j)}, \theta_1^{(j)})$. The $\theta_0^{(j)}$ is the probability to measure 0 given that the qubit j was in the state 1, and the $\theta_1^{(j)}$ is the probability to measure 1 given that the qubit was in the state 0. All together, the noisy RESET gate is modeled by

$$\widetilde{RESET}(\rho) \stackrel{\text{def}}{=} \theta_0 |0\rangle \langle 0| \rho |0\rangle \langle 0| + \theta_1 |0\rangle \langle 1| \rho |1\rangle \langle 0|
+ (1 - \theta_0) |1\rangle \langle 0| \rho |0\rangle \langle 1| + (1 - \theta_1) |1\rangle \langle 1| \rho |1\rangle \langle 1|.$$
(23)

B. Classical optimization

The minimization of the cost function $\Phi(\theta)$ in Eqs. (14, 18) was done using the stochastic optimization algorithm Adam [50], implemented by PyTorch with an automatic differentiation engine [51]. We used the same numerical optimization procedure for both the numerical simulations and the experimental results on real quantum hardware. This is because the cost function depends only on the local expectation values, which may come either from numerical simulations or actual experiments.

Heuristically, we fixed the maximum number of optimization steps to be 15,000. We added another heuristic termination criterion for the optimization process, wherein the optimization ceased if at step i, the difference in the loss function from step i-500 was less than 0.25%.

In what follows, we denote by θ_{est} the channel parameters which achieve the lowest cost function value of $\Phi(\theta_{est})$.

V. NUMERICAL SIMULATIONS

To test our method, we performed several numerical simulations of the stochastic and deterministic maps, and optimized over the cost function to learn the underlying noise model. Below, we briefly describe the technical details of simulations, followed by their results.

A. Simulation of the dynamics and calculation of the expectation values

For both maps, we simulated systems of n=5 to n=11 qubits arranged on a line, with the initial state $\rho_0=|0\rangle\langle 0|^{\otimes n}$. The simulations were done by evolving the full density-matrix on a computer. An approximation for steady state ρ_{∞} of a quantum channel \mathcal{E} was obtained numerically by iteratively applying the quantum channel until the convergence criteria $D(\rho_t, \mathcal{E}(\rho_t)) \stackrel{\text{def}}{=} \frac{1}{2} \|\rho_t - \mathcal{E}(\rho_t)\|_1 < 10^{-6}$ was reached. The approximate steady-state was then used to calculate the expectation values of the local Pauli operators in the different cost functions $\Phi(\theta)$, as given in Eq. (9).

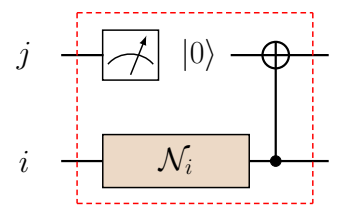


FIG. 4. Structure of the RESCX $(i \to j)$ gate acting two neighboring qubits j, i. We first break the entanglement between i, j by resetting qubit j, and then recreate some entanglement between them by applying $CX(i \to j)$. During the action of the RESET gate on qubit j, the idle noise channel \mathcal{N}_i is acting on qubit i.

We modeled the statistical noise in the expectation value of the local observables using a Gaussian random variable that approximates the binomial distribution of measurement results. For an observable A that is a product of Pauli matrices, it is easy to verify that the statistical noise of N shots is well approximated by a Gaussian random variable $S \sim \mathcal{N}(0,\sigma)$ with $\sigma = \sqrt{(1-\langle A \rangle_{\infty}^2)/N}$.

B. Stochastic map simulations

For the stochastic map simulations, our noise model consisted of dephasing (in the \hat{z} direction) and amplitude damping, as well as the noisy RESET gate from Eq. (23). This amounts to 4 noise parameters for each qubit: 2 for the dephasing and amplitude damping and 2 for the noisy RESET gate. In all unitary gates, we assumed no coherent errors. The exact form of the Lindbladian dissipators is given in Appendix B 2.

We simulated 3 different stochastic maps, which used the same local channels but with different probabilities $\{p_k\}$. We refer to them as probability set 1, 2, and 3.

The set of gates that defined the stochastic map consisted of the single-qubits gates $X^{1/2}$, H, $R_{\alpha}(\psi)$, and a non-unitary 2-local gate between neighboring qubits i,j, which we call RESCX($i \rightarrow j$). The $R_{\alpha}(\psi)$ gate is a single-qubit rotation gate by an angle ψ around the axis α , and RESCX($i \rightarrow j$) is discussed below.

Following the IBMQ hardware specifications, the $R_{\alpha}(\psi)$ gate was implemented as a combination of two $X^{1/2}$ and three $R_{z}(\phi_{i})$ gates, which are native gates in IBMQ:

$$R_{\alpha}(\psi) = R_{z}(\phi_1)X^{1/2}R_{z}(\phi_2)X^{1/2}R_{z}(\phi_3),$$
 (24)

In the formula above, the three rotation angles $\{\phi_i\}_{i=1}^3$ implicitly define the rotation angle ψ and the rotation axis α .

The RESCX $(i \to j)$ gate is a combination of the RESET gate on j, followed by a CX $(i \to j)$, as shown in Fig. 4. The motivation behind this construction is that the RESET gate makes the quantum channel non-unital, but also breaks entanglement. This might lead to

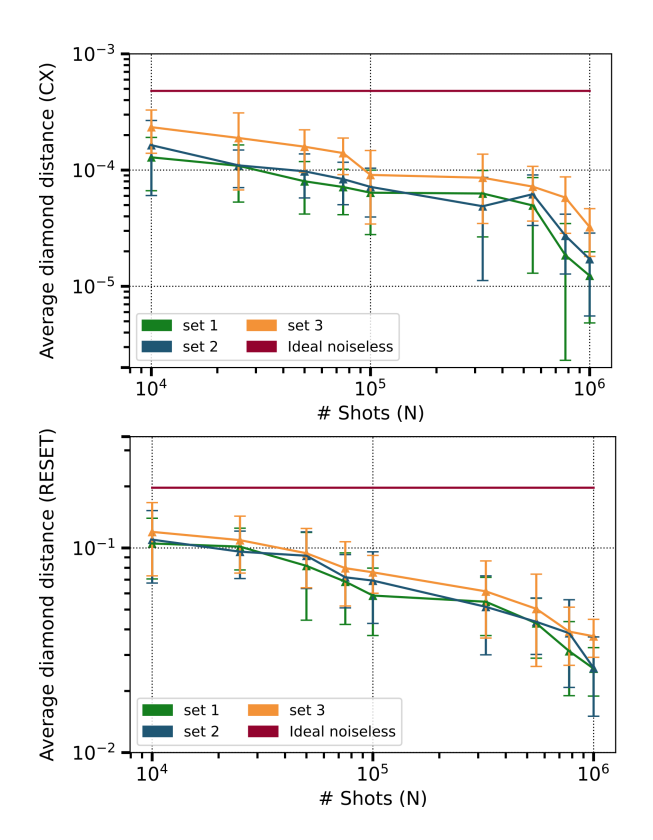


FIG. 5. The average diamond distance between the noisy CX and RESET gates, for a fixed system size n=6 qubits. Each data point being the average of 10 statistical noise realizations in the expectation values. The error bars indicate the uncertainty of two standard deviations. (Top): The average diamond distance for the CX gates. (Bottom): The average diamond distance for the RESET gates. Each color represents a different probability set $\{p_k\}$. The constant horizontal line (red color) represents the diamond distance between the ideal case of the noiseless channel and the true noise channel parameters.

a trivial steady-state, from which it is hard to learn the underlying noise model. Applying the $\mathrm{CX}(i \to j)$ gate right after the RESET(j) was applied regenerates some entanglement.

The full description of the 3 probability sets, together with the underlying noise model, the gates and their execution times, are given in Appendix B.

Our three probability sets were chosen such that the probability of picking a certain gate is independent of the qubit on which it acts. Taking the time scale T_0 (see also Sec. IV A) to be the maximum running time over the gate set $\{X^{1/2}, H, R_{\alpha}(\psi), \text{RESCX}\}$, the implementation of the stochastic channel from Sec. III B on a quantum computer, is described by the following algorithm:

- 1. Pick a gate $1 \le k \le 4$ from the set $\{X^{1/2}, H, R_{\alpha}(\psi), \text{RESCX}\}\$ with probability p_k .
- 2. If the chosen gate is a single-qubit unitary, uniformly choose a qubit and apply it.

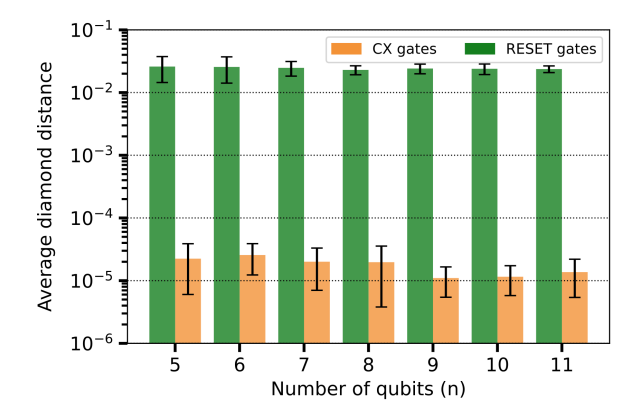


FIG. 6. The average diamond distance between the noisy CX and RESET gates, for a fixed number of shots $N=10^6$, using the probabilities $\{p_k\}$ from the set 2. Each data point being the average of 10 statistical noise realizations in the expectation values. The error bars indicate the uncertainty of two standard deviations.

- 3. If the chosen gate is the RESCX gate, uniformly choose a neighboring pair of control and target qubits and apply it.
- 4. If the total running time T of the chosen gate from steps 2 or 3 is smaller than T_0 , wait $\Delta T = T_0 T$.

Following the discussion in Sec. III B, we chose the observables A in the cost function (14) to be all possible, geometrically 2-local Pauli operators. Consequently, the optimization procedure used the expectation values of 3-local Paulis.

To evaluate the accuracy of the numerical optimization, we calculated the diamond distance between the original noisy CX and RESET gates and the ones obtained from the optimization routine. We focused on these two gates because they have the longest gate times, and therefore they are the most noisy gates in the simulation.

Fig. 5 and Fig. 6 present the average diamond distance between the noisy CX and RESET gates. For a system of size n, the average is taken over n possible RESET gates and 2(n-1) possible CX gates. Fig. 5 shows the average diamond distance as a function of the number of shots per local Pauli observable, with the system size fixed at n=6 qubits. The results are robust for the three different probability sets.

With $N=10^6$ shots per Pauli observable, the average diamond distance for the CX gate is approximately 2×10^{-5} , while the average diamond distance for the RESET gates is of the order 2×10^{-2} . The difference between these two distances is probably because the noise parameters that determine the noisy CX affect not only the RESCX gate, but also the idle noise channels and the noisy single qubit gates. In contrast, the noise parameters of the RESET gate appear only when the RESCX gate is applied.

The same behavior can be observed in Fig. 6, where we

present the average diamond distance as a function of the number of qubits in the system using 10^6 measurements per local Pauli operator for the probability set 2.

It would be interesting to find the *optimal* choice of the gates and probability distribution $\{p_k\}$ for learning a given model of noise. We leave this for future works.

C. Deterministic maps simulations

1. The RESU gate

As mentioned in Sec. III C, we realized the 2-local nonunital channels $\{\mathcal{E}_k\}$ of the deterministic maps using a composed gate called the RESU gate. As shown in Fig. 2, the RESU gate on qubits k, k+1 consists of two 2-local unitaries $U_{k,1}$ and $U_{k,2}$ acting on qubits k, k+1 along with a RESET gate on qubit k:

$$RESU_k \stackrel{\text{def}}{=} U_{k,2} \cdot (RESET_k \otimes \mathbb{I}_{k+1}) \cdot U_{k,1}. \tag{25}$$

Each of the unitaries $U_{k,i=1,2}$ is made of a CX gate and two arbitrary single-qubit rotation gates. Therefore, different RESU gates are characterized by four single-qubit rotations $R_{\alpha}(\psi)$, which we denote by $\{\alpha_k, \psi_k\}_{k=1}^4$. As in Sec. VB, each single-qubit rotation $R_{\alpha}(\psi)$ is implemented as a product of two $X^{1/2}$ and three $R_{z}(\phi_i)$ gates, as described in Eq. (24).

To model the noise in the deterministic map, we used the framework of Sec. IV A. For each unitary $U_{k,i=1,2}$ in we defined its noisy version $\tilde{U}_{k,i=1,2}$ by replacing its noiseless composing gates by their noisy versions. The noisy CX gates in $\tilde{U}_{k,i=1,2}$ were modeled by Eq. (21), and the noisy single-qubit rotations $R_{\alpha}(\psi)$ were modeled by Eq. (22). Finally, the noisy RESET gate is modeled by Eq. (23). Together, the expression of the noisy RESU gate becomes:

$$RESU_{k} \stackrel{\text{def}}{=} \tilde{U}_{k,2} \cdot (R\widetilde{ESET}_{k} \otimes \mathcal{N}_{k+1}) \cdot \tilde{U}_{k,1}, \qquad (26)$$

where \mathcal{N}_{k+1} is an idle noise channel on qubit k+1 for the duration of the noisy RESET gate.

For the time scale T_0 , as defined in Sec. IV A, we took the maximum running time over all {RESU_k} gates. For any RESU_k gate with the running time $T_k < T_0$, a twoqubit idle noise channel $\mathcal{N}_k \otimes \mathcal{N}_{k+1}$ is applied for the duration $\Delta T_k = T_0 - T_k$. On a real QC the idle noise channel is replaced by the *delay* instruction.

2. Numerical results

We simulated three deterministic maps, which we refer to as map-1, map-2, and map-3. Each map used two different RESU gates: one for the even layer, and one for the odd layer. In each layer, the same RESU gate was used on all qubits. We note that while the general RESU gate is defined by four single-qubit rotations $R_{\alpha}(\psi)$, the

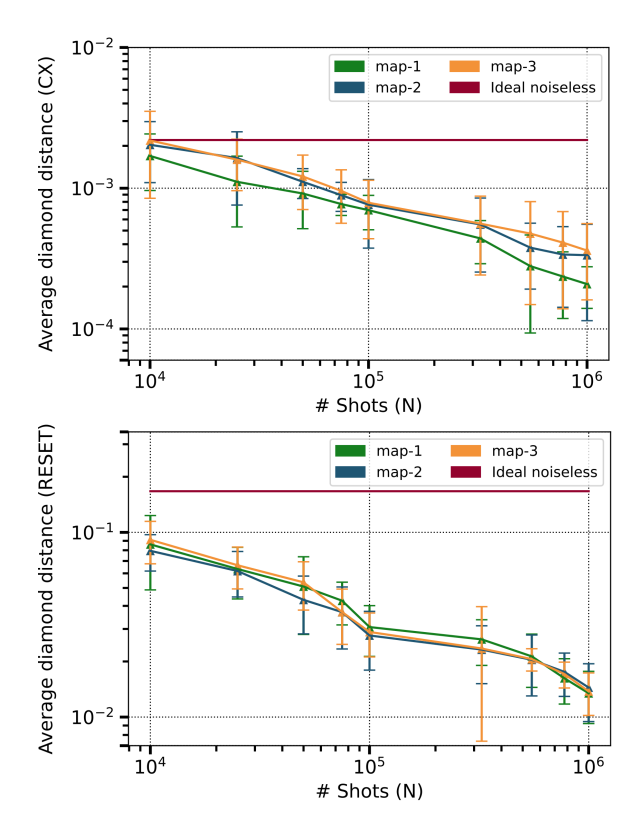


FIG. 7. The average diamond distance between the noisy CX and RESET gates, for a fixed system size n=8 qubits. Each data point being the average of 10 statistical noise realizations in the expectation values. The error bars indicate the uncertainty of two standard deviations. (Top): The average diamond distance for the CX gates. (Bottom): The average diamond distance for the RESET gates. Each color represents a different maps defined by the rotation axes and angles, $\{\alpha_k, \psi_k\}_{k=1}^4$. For a specific map, the pairs $\{\alpha_k, \psi_k\}$ were randomly generated, and kept constant. The constant horizontal line (red color) represents the diamond distance between the ideal case of the noiseless channel and the true noise channel parameters.

actual gates used in the simulations and experiments only used two single qubits rotations in each gate by setting $R_{\alpha}=R_{\beta}$ and $R_{\gamma}=R_{\delta}$ (see Fig. 2). This was due to a technical reason: limiting the number of parameters helped us to find sets of angles for which the convergence to the steady state was rapid (as required by the IBMQ hardware). All together, each deterministic map was defined by a set of 4 single-qubit rotations (2 for the even layer RESU and 2 for the odd layer RESU). The full details of the maps, including the rotation axes and angles, as well the different gate times, are described in Appendix C.

The noise model we used in the simulations of the deterministic maps consisted of generalized amplitude damping and non-uniform depolarization. For each qubit this amounted to 5 Lindblad operators: 3 depolarization operators (one for each axis) and two operators for the generalized amplitude damping [52–54]. In addition, for

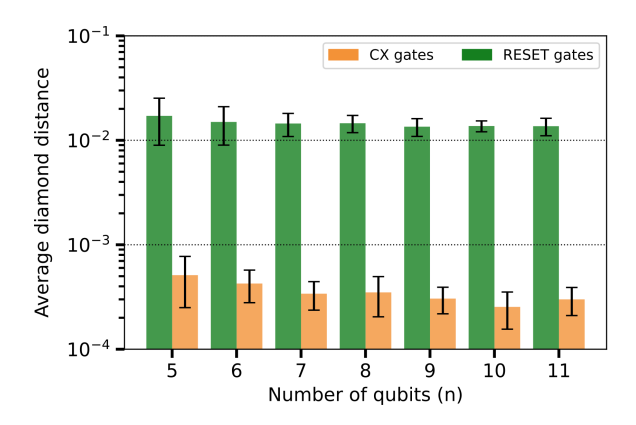


FIG. 8. The average diamond distance between the noisy CX and RESET gates, for a fixed number of shots $N=10^6$, using the rotations $\{\alpha_k, \psi_k\}$ from the map 2. Each data point being the average of 10 statistical noise realizations in the expectation values. The error bars indicate the uncertainty of two standard deviations.

each qubit we had two parameters modeling its RESET gate according to Eq. (23). As in the stochastic case, we assume no coherent errors in the unitary gates. The full description of the noise model is given in Appendix C 2.

After running the simulations, we learned the noise model using the optimization procedure of Sec. IV B. To evaluate the accuracy of the noise parameter estimation, we used the same procedure as in the stochastic maps simulations, and compared the noisy CX and RESET gates used in the simulations to the ones obtained from the optimization routine.

In Fig. 7 and Fig. 8, the average diamond distance between the noisy CX and RESET gates used in the simulations and those obtained from the optimization is presented. For a system of size n, the average is taken over the n-1 possible RESET gates and 2(n-1) possible CX gates.

In Fig. 7, we present the average diamond distance as a function of the number of shots per local Pauli observable for a fixed system size of n=8 qubits, using three randomly generated sets of rotation axes and angles, $\{\alpha_k, \psi_k\}_{k=1}^4$. Each of the three sets resulted in a different steady state. The accuracy of the estimation is robust to the different sets of rotation angles and axes (which are given in Appendix C1). For $N=10^6$ shots per local Pauli observable, the average diamond distance for the CX gates is approximately 3×10^{-4} , while for the RESET gates it is approximately 1.4×10^{-2} .

In Fig. 8 we kept the number of shots per Pauli fixed at $N=10^6$ and used the rotation angles and axes from map 2. Increasing the system size from n=5 to n=11, we observe that the accuracy of the parameter estimation improves slightly between n=5 and n=7, and remains robust up to n=11. The initial increase in accuracy for smaller systems in Fig. 8 may be explained by examining the light cone shown in Fig. 3 in Sec. III C. For a smaller system size with open boundary conditions, the

light cone is truncated at each end of the system, causing the expectation values at the edges of the system to be 3-local instead of 4-local. As a result, the optimization routine uses fewer statistics for the qubits located at the ends of the system. However, for larger system sizes, this boundary effect becomes negligible as the relative fraction of boundary qubits decreases.

As in the case of the stochastic map in Sec. VB, the average diamond distance for the CX gates is much smaller than the RESET gates. This is probably because the noise channel parameters within the CX gates appear in multiple combinations within a single RESU gate, while the channel parameters of the RESET gate only appear once per RESU gate.

VI. QUANTUM DEVICE RESULTS

In this section we describe the experiments we performed on actual quantum hardware to test our method. All experiments were done on an IBMQ machine via the IBMQ cloud.

A. Details of the experiment

For the quantum hardware demonstration we chose the ibm_lagos v1.0.32, which is one of the IBM Quantum Falcon Processors [55] with 7 qubits in the shape of a rotated H. Out of the 7 qubits, we chose n=5 qubits arranged in a line, which we labeled by 0,1,2,3,4. The IBMQ labels of these qubits were 6,5,3,1,0 in corresponding order.

We used the deterministic map-1 in Sec. III C to learn the noise of the quantum hardware. See Appendix C 1 for an exact description of the map. Our noise model was the same model used in the deterministic map simulations, which consisted of non-uniform depolarization errors, generalized amplitude damping, and RESET errors (total of 7 free parameters per qubit). In addition to these parameters we added a modeling of coherent CX errors as free parameters in its Hamiltonian — see Appendices A, C 2 for a full description of the model.

After learning the hardware noise model using map-1, we ran deterministic map-2 and measured 2-local Pauli expectation values on its steady state. We used these measurements to test the quality of the noise model we learned from map-1.

To reduce SPAM errors, we used a readout-error mitigation scheme, which was partially based on Refs. [56, 57]. The scheme relied on a preliminary step in which we estimated the conditional probability of measuring a 4-local bit string in the computational basis, assuming the qubits were prepared in a different computational basis. See Appendix D 1 for an full description of our scheme.

Overall, our experiment consisted of three steps: (i) preliminary readout-error mitigation measurements, (ii) running deterministic map-1 and measuring the expectation values of 4-local Paulis, and (iii) running deter-

ministic map-2 and measuring the expectation values of 2-local Paulis.

In all three parts of the experiment we needed to estimate the expectation values of local Pauli strings. To that aim, we used the overlapping local tomography method, described by Zubida $et\ al.$ in Ref. [8], which simultaneously estimates all geometrically k-local Pauli strings using a set of 3^k different measurement circuits. This means that using a total budget of M shots, each Pauli string was estimated using $M/3^k$ shots.

We now describe the 3 parts of the experiment in more details.

(i) Readout error mitigation measurements: Here we performed preliminary readout-error mitigation measurements for the protocol that is described in Appendix D 1. Our measurements were used to mitigate the readout errors of steps (ii),(iii). We used the overlapping local tomography method (see Zubida et al. in Ref. [8]), to obtain 4-local readout statistics from a set of 2^4 different measurement circuits of unit depth. On each circuit we performed 2×10^5 measurements (about $M=3\times 10^6$ shots in total).

(ii) 4-local channel measurements: In this step we ran the deterministic map-1 on the quantum computer and prepared many copies of the steady states of \mathcal{E}_I and \mathcal{E}_{II} channels. Following the numerical simulations, we assumed that the steady state of each channel was approximately reached after 10 steps. We then used the overlapping local tomography to estimate the expectation values of the 4-local Pauli operators using 1.25×10^5 measurements for every 4-local expectation value (and about $M=2\times 10^7$ shots in total).

(iii) 2-local channel measurements: In this step we ran the deterministic map-2 on the quantum computer and performed 2-local Pauli measurements using the overlapping local tomography. As explained in Sec. V C, map-2 produces a different steady state from the map-1. We used these 2-local Pauli measurements to asses the accuracy of our noise model we learned from the 4-local expectation values of step (ii). As in part (ii), we assumed that the steady states of the \mathcal{E}_I and \mathcal{E}_{II} channels were approximately reached after 10 steps. The 2-local Pauli expectation values were obtained using overlapping local tomography that used 1.25×10^5 measurements for every 2-local expectation value (and about $M = 2 \times 10^6$ shots in total).

Upon finishing the measurements in (ii), (iii), we used the results of readout measurements (i) to correct these measurement statistics (see Appendix D 1 for details).

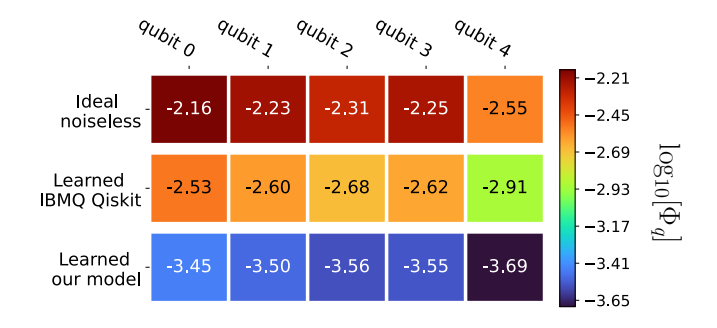


FIG. 9. The cost map for the *ibm_lagos* device for three noise models: the ideal noiseless case (top row), the learned noise model from IBMQ Qiskit backend (middle row), and the learned noise model using our method (bottom row).

B. Results I: Noise model validation

The main application of our method is to validate (benchmark) a noise model of a QC by calculating its local cost functions Φ_q given a noise model that defines the noisy channels $\{\tilde{\mathcal{E}}_k\}$, as explained in Sec. III C. The local cost function Φ_q for a qubit q is the sum of all the A_j entries in Φ_I and Φ_{II} (see Eq. (17)) that overlap qubit q, divided by the number of such A_j . This happens when the light cone of A_j includes qubit q, i.e., when $q \in \{j-1, \ldots, j+2\}$ (see Fig. 3 for an illustration).

We used our validation protocol to compare three noise models: (i) the ideal noiseless model, (ii) our estimate of the IBMQ Qiskit [58] noise model, imported from the device's backend properties at the time of our experiment, and (iii) a noise model that we learned from the IBMQ hardware using our optimization method (see Sec. IV).

To calculate model (ii), we needed to know $\mathcal{E}^*_{odd}, \mathcal{E}^*_{even}$ of the IBMQ Qiskit noise model, from which the local cost function is calculated (see Eqs. (15, 16, 17)). However, as far as we could tell, IBMQ does not fully publish the exact formulas it uses to model the local noise. Instead, it publishes general noise parameters such as T_1, T_2 , and provides code that simulates noisy circuits. Therefore, in order to calculate \mathcal{E}_{odd}^* , \mathcal{E}_{even}^* , we first learned IBMQ Qiskit noise model using the deterministic map-3, and used the resultant model as an approximation to IBMQ Qiskit noise model. In more details, we used IBMQ Qiskit simulator to simulate the steady state of map-3, and calculated local Pauli expectations with vanishing statistical noise. We then used our optimization routine to learn Qiskit's noise model. We used the parameters described in Appendix C2, but without any coherent errors, and with depolarization only along the \hat{z} axis. As a sanity check, we used the model we learned to simulate the 5 qubits steady states of maps-1,2,3 and compared them to Qiskit's steady states. We noticed that in all cases the trace distance between our steady state and Qiskit's steady state was less than 1%.

Fig. 9 shows the single-qubit cost function, as a heat map. The different rows represent $\log_{10}\Phi_q$ for the 3 noise

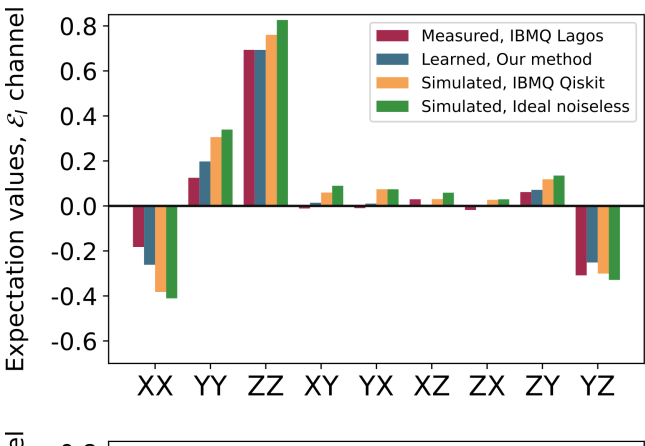
models. Unsurprisingly, it suggests that IBMQ Qiskit's noise model provides a better description of the hardware than the ideal, noiseless channel. It also suggests that our estimated noise model performs significantly better than the two other models. This might not be surprising, given the fact that we learned our noise model using the same steady state that we used to validate it. In other words, the learned noise model parameters are the ones that minimize the global cost function, which is roughly the sum of the local cost functions that appear in Fig. 9. In the machine learning jargon, this might imply that our noise model estimation procedure overfitted the particular steady state from which the 4-local measurements were sampled. To rule this out (at least to some extent), we show in the next subsection that our estimated noise model has a better predictive power than the other two: it is able to better approximate the 2-local expectation values of a steady state of map-2, which is different from the steady state of map-1 with which we learned the noise model.

C. Results II: Noise model characterization

In this section we present the results of applying our optimization algorithm to *characterize* the noise within a quantum device. The full learned noise model parameter details are presented in Appendix D 2.

To evaluate the quality of our noise characterization, we took the noise model that we learned and used it to numerically simulate the steady states of map-2 (of \mathcal{E}_I and \mathcal{E}_{II}). On these steady states we calculated the expectation values of 2-local Paulis in the bulk of the 5qubits line (we used qubits 1, 2 for \mathcal{E}_I and 2, 3 for \mathcal{E}_{II}). We then compared these simulated expectation values to the actual results we measured on the quantum hardware when running map-2 (part (iii) of our experiment described in Sec. VIA). We used the same procedure to test the two other noise models from the previous section, i.e., the ideal (noiseless) model, and IBMQ Qiskit's model. In contrast to the previous section, to sample the 2-local Paulis from the IBMQ Qiskit noise model we don't need to know \mathcal{E}_{odd}^* , \mathcal{E}_{even}^* . Hence, we calculated the 2-local Pauli expectation values directly from the IBMQ Qiskit simulator using the noise model imported from the device's backend properties at the time of our experiment.

Our results are presented as histograms in Fig. 10, where we show the expectation values of the 9 possible 2-local Pauli expectation values for the steady states of \mathcal{E}_I , \mathcal{E}_{II} of map-2. The expectation values from the quantum hardware are shown in red. As we used more than 10^5 measurements for each data point, the statistical error is smaller than 0.005, which is negligible comparing to the differences with respect to other models. For the 3 analytical models, we preset the exact expectation values, without any statistical error. Our model prediction is shown in blue, Qiskit's model in yellow and the noise-



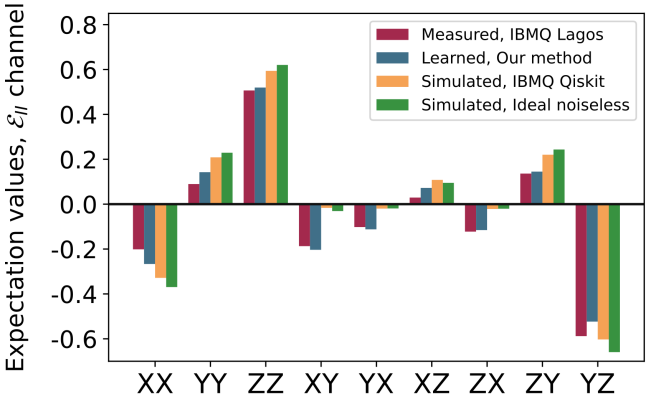


FIG. 10. Expectation values of the 2-local Pauli operators obtained from: the ibm_lagos device (red), the learned noise model using our method (blue), the IBMQ Qiskit simulator (yellow) and the ideal noiseless case (green). We focus on qubits 1,2 for \mathcal{E}_I (top) and 2,3 for \mathcal{E}_{II} (bottom) to avoid including the boundary qubits 0 and 4, for which the measurement statistics become 3-local instead of 4-local (see Sec. V C). See Table I for the corresponding trace distances between the measured RDM and the RDMs of the three models.

less model in green. As can be seen in the figure, while the predictions of all the models are in decent agreement with the empirical results, our model is in better agreement than the other two models.

To compare our estimate in a quantitative way, we used the 2-local Paulies expectation values of the IBMQ hardware to perform quantum state tomography and estimate the underlying 2-local reduced density matrices (RDMs) in the steady states of \mathcal{E}_I , \mathcal{E}_{II} of map-2. We compared it to the RDMs produced by simulations of our model, the Qiskit model and the ideal model. For each case, we calculated the trace distance $D(\rho,\sigma) \stackrel{\text{def}}{=} \frac{1}{2} \|\rho - \sigma\|_1$ between the simulation and the estimated RDM of the IBMQ hardware. The results are given in Table I, showing that indeed the trace distance between IBMQ RDMs and our model RDMs are 50% - 70% of the distances from ideal model or the Qiskit model.

It is worth noting that the 2-local Pauli operators used for the reliability assessment were collected after the 4-

local Pauli expectation values used for noise model characterization were obtained. As a result, the noise model at the time of the 2-local Pauli measurements may have undergone some drifting. This may account for some of the variations seen in the 2-local expectation values depicted in Fig. 10 [59–61].

	\mathcal{E}_I	\mathcal{E}_{II}
Ideal model	0.19	0.21
Qiskit model		
Learned model	0.09	0.13

TABLE I. The trace distance of the 2-local reduced density matrices obtained from the IBMQ hardware using quantum state tomography and the corresponding density matrices taken from simulations using the ideal model, Qiskit noise model, and our learned model. We calculated the distances on the steady states of \mathcal{E}_I and \mathcal{E}_{II} of map-2.

VII. SUMMARY AND OUTLOOK

We have presented and demonstrated numerically and experimentally a new framework for benchmarking a quantum computer by driving it to a steady state of an engineered dissipative dynamics. It is a natural generalization of the recent results of learning a local Hamiltonian or Lindbladian from their steady states [24–27].

We have shown that if the underlying dissipative map is Markovian and local, then there exist a set of linear constraints between the expectation values of local observables in the steady state. This steady state can be a correlated, entangled state, and might even be classically inaccessible. Nevertheless, as we showed, the constraints between its local expectation values are local and can be efficiently verified once we measure these expectation values. We can therefore apply our method to a system with a large number of qubits and test how well a given noise model globally describes the system, which is in a state that might be classically inaccessible.

For generic dissipative maps, the steady state is unique, and consequently, our method is independent of the initial state and is insensitive to state preparation errors. In addition, the fact that we measure a steady state that was created using several iterations allows us to test for the possible deviations from the Markovian model, in the form of memory and temporal correlations. Finally, by optimizing over a parametrized set of local Markovian noise models, our method allows learning of the optimal noise model.

We have suggested two generic ways to engineer a dissipative map on a quantum computer, both of which rely on the non-unital RESET gate. The first is a stochastic map that is implemented on a quantum computer by applying a set of gates according to a prescribed probability distribution. The second, uses a brick-wall type

circuit, whose building blocks are composed 2-local non-unital gates and can therefore be applied using a single circuit. We have demonstrated numerically both methods using simulations of 5-11 qubits, and showed that it can successfully learn an underlying noise model. In our numerical tests we managed to learn the underlying CNOT and RESET gates up to diamond distances of $10^{-3}-10^{-5}$ and $10^{-1}-10^{-2}$ respectively, using 10^4-10^6 shots per observable.

We have also tested our method experimentally on on the IBMQ *ibm_lagos* machine using 5 qubits. We have shown that given a noise model, we can construct a 'heat map' view of the qubits showing how well the model describes each qubit. Our method clearly showed that IBMQ Qiskit's simplified noise model performs better than the ideal, noiseless model. Finally, we have also showed how our method can learn an underlying noise model for that machine, and that the model it learned better predicted the outcomes of another experiment than the noiseless model or IBMQ Qiskit's model.

Our work leaves several theoretical and practical questions. On the theoretical side, it would be interesting to characterize the complexity of the steady states of dissipative maps like the one we used. Can they be sampled classically, or can they encode some BQP hard problems? More general engineered dissipative maps are known to be BQP-complete [37], but our maps are much simpler. They also differ from the much studied class of randomly generated circuits, for which there are several complexity bounds (see, for example, the recent result in Ref. [62] and references within), in several aspects: our maps are not completely random (we apply the same map over and over), they are strongly dissipative and non-unital, and can be applied for poly(n) time.

It would also be interesting to find a systematical way of engineering the dissipative maps (of both types) to have an optimal estimate of the error parameters. This might be possible to do by studying the quantum Fisher information [63] of the steady states with respect to the free parameters of the map. Related to that, it would be interesting to understand how this the quantum Fisher information, or more general our ability to use the steady state for learning, depends on the deviation of the channel from unitarity. Is there a phase transition behavior, as seen in related measurement induced phase transitions literature (see Ref. [64] and references within), or is it a smooth transition?

On the more practical direction, it would be interesting to see if there is a way to make our method completely insensitive to SPAM errors, by removing its dependence of measurement errors. The readout error mitigation procedure that we employed arguably removes a large part of these errors, but not in a controlled, systematic way, as done in methods like RB [38–41] and GST [42–44].

ACKNOWLEDGEMENTS

We thank Eyal Bairey and Netanel Lindner for enlightening discussions. IA acknowledges the support of the Israel Science Foundation (ISF) under the Research Grants in Quantum Technologies and Science No. 2074/19, and the joint NRF-ISF Research Grant No. 3528/20. This research is supported by the National Research Foundation, Singapore, under its Quantum Engineering Programme. We are very grateful for the support of the National University of Singapore (NUS) and the Centre of Quantum Technologies (CQT) for their help in running the IBMQ experiments.

- D. Burgarth, K. Maruyama, and F. Nori, Phys. Rev. A 79, 10.1103/PhysRevA.79.020305 (2009), arXiv:0810.2866.
- [2] C. Di Franco, M. Paternostro, and M. S. Kim, Phys. Rev. Lett. 102, 10.1103/PhysRevLett.102.187203 (2009), arXiv:0812.3510.
- [3] A. Shabani, M. Mohseni, S. Lloyd, R. L. Kosut, and H. Rabitz, Phys. Rev. A 84, 10.1103/Phys-RevA.84.012107 (2011), arXiv:1002.1330.
- [4] M. P. Da Silva, O. Landon-Cardinal, and D. Poulin, Phys. Rev. Lett. 107, 10.1103/PhysRevLett.107.210404 (2011), arXiv:1104.3835.
- [5] J. Zhang and M. Sarovar, Phys. Rev. Lett. 113, 80401 (2014).
- [6] L. E. De Clercq, R. Oswald, C. Flühmann, B. Keitch, D. Kienzler, H. Y. Lo, M. Marinelli, D. Nadlinger, V. Negnevitsky, and J. P. Home, Nat. Comm. 7, 10.1038/ncomms11218 (2016), arXiv:1011.1669v3.
- [7] Y. Wang, D. Dong, B. Qi, J. Zhang, I. R. Petersen, and H. Yonezawa, IEEE Transactions on Automatic Control 63, 1388 (2018), arXiv:1610.08841.
- [8] A. Zubida, E. Yitzhaki, N. H. Lindner, and E. Bairey, arXiv e-prints, arXiv:2108.08824 (2021), arXiv:2108.08824 [quant-ph].
- [9] C. Kokail, R. van Bijnen, A. Elben, B. Vermersch, and P. Zoller, Nature Physics 17, 936 (2021).
- [10] W. Yu, J. Sun, Z. Han, and X. Yuan, arXiv e-prints, arXiv:2201.00190 (2022), arXiv:2201.00190 [quant-ph].
- [11] F. Wilde, A. Kshetrimayum, I. Roth, D. Hangleiter, R. Sweke, and J. Eisert, arXiv , 1 (2022), arXiv:2209.14328.
- [12] H. J. Kappen, Journal of Physics A: Mathematical and Theoretical 53, 214001 (2020).
- [13] A. Anshu, S. Arunachalam, T. Kuwahara, and M. Soleimanifar, Nature Physics 17, 931 (2021).
- [14] J. Haah, R. Kothari, and E. Tang, arXiv e-prints, arXiv:2108.04842 (2021).
- [15] Y. Y. Lifshitz, E. Bairey, E. Arbel, G. Aleksandrowicz, H. Landa, and I. Arad, arXiv e-prints, arXiv:2112.10418 (2021), arXiv:2112.10418 [quant-ph].
- [16] C. E. Granade, C. Ferrie, N. Wiebe, and D. G. Cory, New Journal of Physics 14, 10.1088/1367-2630/14/10/103013 (2012), arXiv:1207.1655v1.
- [17] N. Wiebe, C. Granade, C. Ferrie, and D. G. Cory, Phys. Rev. Lett. 112, 10.1103/PhysRevLett.112.190501 (2014), arXiv:1309.0876.
- [18] N. Wiebe, C. Granade, C. Ferrie, and D. Cory, Phys. Rev. A 89, 10.1103/PhysRevA.89.042314 (2014), arXiv:1311.5269.
- [19] N. Wiebe, C. Granade, and D. G. Cory, New Journal of Physics 17, 10.1088/1367-2630/17/2/022005 (2015), arXiv:1409.1524.

- [20] J. Wang, S. Paesani, R. Santagati, S. Knauer, A. A. Gentile, N. Wiebe, M. Petruzzella, J. L. O'brien, J. G. Rarity, A. Laing, and M. G. Thompson, Nat. Phys. 13, 551 (2017), arXiv:1703.05402.
- [21] A. Sone and P. Cappellaro, Physical Review A 95, 1 (2017), arXiv:1609.09446.
- [22] M. Greiter, V. Schnells, and R. Thomale, Phys. Rev. B 98, 081113 (2018).
- [23] E. Chertkov and B. K. Clark, Phys. Rev. X 8, 031029 (2018).
- [24] X.-L. Qi and D. Ranard, Quantum 3, 159 (2019).
- [25] E. Bairey, I. Arad, and N. H. Lindner, Phys. Rev. Lett. 122, 020504 (2019).
- [26] E. Bairey, C. Guo, D. Poletti, N. H. Lindner, and I. Arad, New Journal of Physics 22, 10.1088/1367-2630/ab73cd (2020), arXiv:1907.11154.
- [27] T. J. Evans, R. Harper, and S. T. Flammia, arXiv e-prints , arXiv:1912.07636 (2019), arXiv:1912.07636 [quant-ph].
- [28] Strictly speaking, this is true up to an overall factor.
- [29] L. Del Re, B. Rost, A. F. Kemper, and J. K. Freericks, Phys. Rev. B 102, 125112 (2020).
- [30] G. García-Pérez, M. A. C. Rossi, and S. Maniscalco, npj Quantum Information 6, 1 (2020).
- [31] S. Sun, L.-C. Shih, and Y.-C. Cheng, arXiv e-prints, arXiv:2106.12882 (2021), arXiv:2106.12882 [quant-ph].
- [32] B. Rost, L. Del Re, N. Earnest, A. F. Kemper, B. Jones, and J. K. Freericks, arXiv e-prints, arXiv:2108.01183 (2021), arXiv:2108.01183 [quant-ph].
- [33] T. J. Sewell and S. P. Jordan, arXiv e-prints , arXiv:2109.09787 (2021), arXiv:2109.09787 [quant-ph].
- [34] S. Tornow, W. Gehrke, and U. Helmbrecht, Journal of Physics A: Mathematical and Theoretical 55, 245302 (2022).
- [35] M. Cattaneo, M. A. C. Rossi, G. García-Pérez, R. Zambrini, and S. Maniscalco, arXiv e-prints, arXiv:2201.11597 (2022), arXiv:2201.11597 [quant-ph].
- [36] P. M. Harrington, E. J. Mueller, and K. W. Murch, Nature Reviews Physics 4, 660 (2022).
- [37] F. Verstraete, M. M. Wolf, and J. Ignacio Cirac, Nature Physics 5, 633 (2009).
- [38] J. Emerson, R. Alicki, and K. Życzkowski, Journal of Optics B: Quantum and Semiclassical Optics 7, S347 (2005).
- [39] J. Emerson, M. Silva, O. Moussa, C. Ryan, M. Laforest, J. Baugh, D. G. Cory, and R. Laflamme, Science 317, 1893 (2007), https://www.science.org/doi/pdf/10.1126/science.1145699.
- [40] E. Knill, D. Leibfried, R. Reichle, J. Britton, R. B. Blakestad, J. D. Jost, C. Langer, R. Ozeri, S. Seidelin, and D. J. Wineland, Phys. Rev. A 77, 012307 (2008).
- [41] E. Magesan, J. M. Gambetta, and J. Emerson, Phys. Rev. A 85, 042311 (2012).

- [42] R. Blume-Kohout, J. K. Gamble, E. Nielsen, J. Mizrahi, J. D. Sterk, and P. Maunz, arXiv 10.48550/ARXIV.1310.4492 (2013).
- [43] D. Kim, D. R. Ward, C. B. Simmons, J. K. Gamble, R. Blume-Kohout, E. Nielsen, D. E. Savage, M. G. Lagally, M. Friesen, S. N. Coppersmith, and M. A. Eriksson, Nature Nanotechnology 10, 243 (2015).
- [44] E. Nielsen, J. K. Gamble, K. Rudinger, T. Scholten, K. Young, and R. Blume-Kohout, Quantum 5, 557 (2021).
- [45] K. Head-Marsden, S. Krastanov, D. A. Mazziotti, and P. Narang, Physical Review Research 3, 13182 (2021), arXiv:2005.00029.
- [46] K. R. Fratus, K. Bark, N. Vogt, J. Leppakangas, S. Zanker, M. Marthaler, and J.-M. Reiner, arXiv (2022), arXiv:2210.11371.
- [47] E. van den Berg, Z. K. Minev, A. Kandala, and K. Temme, arXiv (2022), arXiv:2201.09866.
- [48] M. Kjaergaard, M. E. Schwartz, J. Braumuller, P. Krantz, J. I.-J. Wang, S. Gustavsson, and W. D. Oliver, Annual Review of Condensed Matter Physics 11, 369 (2020), https://doi.org/10.1146/annurevconmatphys-031119-050605.
- [49] P. Jurcevic, A. Javadi-Abhari, L. S. Bishop, I. Lauer, D. F. Bogorin, M. Brink, L. Capelluto, O. Günlük, T. Itoko, and N. Kanazawa, Quantum Science and Technology 6, 025020 (2021).
- [50] D. P. Kingma and J. L. Ba, 3rd International Conference on Learning Representations, ICLR 2015 - Conference Track Proceedings , 1 (2015), arXiv:1412.6980.
- [51] A. Paszke, S. Gross, F. Massa, A. Lerer, J. Bradbury, G. Chanan, T. Killeen, Z. Lin, N. Gimelshein, L. Antiga, A. Desmaison, A. Kopf, E. Yang, Z. DeVito, M. Raison, A. Tejani, S. Chilamkurthy, B. Steiner, L. Fang, J. Bai, and S. Chintala, in *Advances in Neural Information Pro*cessing Systems 32 (Curran Associates, Inc., 2019) pp. 8024–8035.
- [52] R. Srikanth and S. Banerjee, Physical Review A Atomic, Molecular, and Optical Physics 77, 10.1103/Phys-RevA.77.012318 (2008), arXiv:0707.0059.
- [53] C. Cafaro and P. Van Loock, Physical Review A -Atomic, Molecular, and Optical Physics 89, 1 (2014), arXiv:1308.4582.
- [54] P. Krantz, M. Kjaergaard, F. Yan, T. P. Orlando, S. Gustavsson, and W. D. Oliver, Applied Physics Reviews 6, 10.1063/1.5089550 (2019), arXiv:1904.06560.
- [55] Ibm quantum. https://quantum-computing.ibm.com/, 2022 (2022).
- [56] M. R. Geller, Quantum Science and Technology 5, 03LT01 (2020).
- [57] M. R. Geller and M. Sun, Quantum Science and Technology 6, 025009 (2021).
- [58] Qiskit: An open-source framework for quantum computing (2022).
- [59] J. M. Chow, J. M. Gambetta, L. Tornberg, J. Koch, L. S. Bishop, A. A. Houck, B. R. Johnson, L. Frunzio, S. M. Girvin, and R. J. Schoelkopf, Physical Review Letters 102, 1 (2009), arXiv:0811.4387.
- [60] M. A. Fogarty, M. Veldhorst, R. Harper, C. H. Yang, S. D. Bartlett, S. T. Flammia, and A. S. Dzurak, Physical Review A - Atomic, Molecular, and Optical Physics 92, 1 (2015), arXiv:1502.05119.
- [61] P. V. Klimov, J. Kelly, Z. Chen, M. Neeley, A. Megrant, B. Burkett, R. Barends, K. Arya, B. Chiaro, and

- Y. Chen, Physical Review Letters 121, 90502 (2018).
- [62] D. Aharonov, X. Gao, Z. Landau, Y. Liu, and U. Vazirani, arXiv e-prints, arXiv:2211.03999 (2022), arXiv:2211.03999 [quant-ph].
- [63] J. J. Meyer, Quantum 5, 539 (2021).
- [64] Y. Li, Y. Zou, P. Glorioso, E. Altman, and M. P. A. Fisher, arXiv e-prints, arXiv:2209.00609 (2022), arXiv:2209.00609 [quant-ph].
- [65] M. Steffen, D. P. DiVincenzo, J. M. Chow, T. N. Theis, and M. B. Ketchen, IBM Journal of Research and Development 55, 13:1 (2011).
- [66] C. Rigetti and M. Devoret, Physical Review B Condensed Matter and Materials Physics 81, 1 (2010).
- [67] M. Malekakhlagh, E. Magesan, and D. C. McKay, Physical Review A 102, 1 (2020), arXiv:2005.00133.
- [68] E. Magesan and J. M. Gambetta, Physical Review A 101, 10.1103/PhysRevA.101.052308 (2020), arXiv:1804.04073.
- [69] A. Kandala, K. X. Wei, S. Srinivasan, E. Magesan, S. Carnevale, G. A. Keefe, D. Klaus, O. Dial, and D. C. McKay, Physical Review Letters 127, 130501 (2021), arXiv:2011.07050.

Appendix A: Modeling the noisy CX

We modeled the noisy CX gate to approximate the actual CX gate available on the IBMQ hardware, which is based on the supercoducting qubits [65]. In IBMQ machines, a two-qubit $CX(i \rightarrow j)$ gate is realized as a microwave-activated two-qubit cross-resonance (CR) gate that consists of driving the control i qubit at the frequency of the target qubit j [66].

Based on the discussions in Refs. [67–69], we modeled the effective Hamiltonian $CX(i \rightarrow j)$ by:

$$H_{\mathrm{CX}(i\to j)} \stackrel{\mathrm{def}}{=} \theta_1^{(ij)} Z_i \otimes X_j - \theta_2^{(ij)} \mathbb{I}_i \otimes X_j - \theta_3^{(ij)} Z_i \otimes \mathbb{I}_j, \tag{A1}$$

where $\theta_{m=1,2,3}^{(ij)}$ are variational parameters that represent the strength for each of the interaction terms. The ideal value for all these parameters is 1, which leads to a CX gate when using dimensionless execution time $T/T_0 = \pi/4$. In reality, these parameters can be different from 1, leading to coherent CX errors. We refer the reader to the Refs. [66–69] for more details on the CR gate implementation on transmons.

Appendix B: Details of the stochastic maps

1. Gates and probabilities

As discussed in Sec. VB, our stochastic maps were defined using the gates RESCX, $X^{1/2}$, H, $R_{\alpha}(\phi)$. We used 3 stochastic maps, defined by 3 probability distributions. In each map, the probability of acting with certain gate was independent of the qubit number. The 3 probability distributions are given in the following table. The parameters of the single-qubit rotations $R_{\alpha}(\phi)$ were chosen randomly.

Gate	RESCX	$X^{1/2}$	Н	$R_{\alpha}(\phi)$
Probability set 1	0.3	0.2	0.2	0.2
Probability set 2	0.5	0.1	0.2	0.2
Probability set 3	0.7	0.1	0.1	0.1

TABLE II. Three different probability distributions $\{p_k\}$ used in the numerical simulations. The rotation axis α and the rotation angle ψ were defined by three rotation angles $\{\phi_i\}_{i=1}^3$ which we randomly generated.

2. Noise model in the stochastic case

In the stochastic case, we used 4 parameters for each qubit to model its noise. We used θ_z, θ_{amp} to model

dephasing and amplitude damping, which are given by the Lindbladians

$$\mathcal{L}_z(\rho) \stackrel{\text{def}}{=} Z\rho Z - \rho,$$
 (B1)

$$\mathcal{L}_{amp}(\rho) \stackrel{\text{def}}{=} \sigma_{+}\rho\sigma_{-} - \frac{1}{2} \{\sigma_{-}\sigma_{+}, \rho\},$$
 (B2)

where

$$\sigma_{\pm} \stackrel{\text{def}}{=} (X \pm iY)/2.$$
 (B3)

In addition, we used θ_0, θ_1 to model the noisy RESET gate, as defined in Eq. (23).

We note that in all the simulations of the stochastic maps, we assumed that the CX gate had no coherent errors; all its errors came from he single-qubit errors of its two-qubits.

For every qubit, the dimensionless noise parameters θ_z , θ_{amp} that we used in our simulations were randomly picked between the values of 0.02 and 0.06. In terms of the coherence times (given by $T_0/\{\theta_m\}$), our choices correspond approximately to a range of 25 [μsec] to 75 [μsec].

The parameters for the noisy RESET were randomly generated between the values 0.87 and 0.98. Following the discussion in Ref. [32], we required $\theta_0 \geq \theta_1$ to match the typical values on the IBMQ hardware. However, we note that the experimentally determined noise parameters of the RESET gates did not follow this assumption.

3. Gate durations

The noisy versions of all single-qubit unitary gates were simulated using Suzuki-Trotter expansion, as outlined in Eq. (22). For the noisy version of the CX we used Eq. (21) with the Hamiltonian defined in Appendix A with vanishing coherent errors.

To define the gate channels in the stochastic map, we used the execution times that resemble the execution times of actual quantum gates in superconducting qubits [48, 49]. For the RESET gates, duration times were generated between $0.8 \, [\mu sec]$ and $1.1 \, [\mu sec]$. For the CX gates, durations were generated between $0.3 \, [\mu sec]$ and $0.45 \, [\mu sec]$. The duration time of the $X^{1/2}$ gate was set to $15 \, [nsec]$, and for the H gate the duration was set to $20 \, [nsec]$. As stated in Sec. VB, the $R_{\alpha}(\psi)$ gate is a product of two $X^{1/2}$ and three $R_{z}(\phi_{i})$ gates. The $R_{z}(\phi_{i})$ gates are implemented on the superconducting platforms, such as IBMQ, with zero error and duration [48]. Therefore, we took the duration of the general single-qubit rotation gate $R_{\alpha}(\psi)$, defined in Eq. (24), to be twice the duration of the $X^{1/2}$ gate.

In our simulations, the time scale T_0 was dictated by duration of the RESCX gate, and was roughly 1.5 [μsec].

Appendix C: Details of the deterministic map

1. Rotation angles in the RESU gates

We used the deterministic map both in numerical simulations and real quantum hardware. Consequently, it was important that the maps we defined will converge to the fixed point in at most 10 steps, which was the maximal number of steps that we could run of these types of circuits on the IBMQ hardware. To that aim, we first ran few numerical simulations to find a combination of rotation angles that will guarantee fast convergence.

Recall from Fig. 2 that the RESU gate is defined by 4 single-qubit rotations, which amounts to 12 rotation parameters per RESET gate (3 parameters for every single-qubit rotation). To facilitate the search for optimal rotation angles (which will give rapid convergence), we reduced this number by half by using the same parameters in the two single-qubit rotations in U_1 (the 2-local unitary before the RESET gate), and similarly in U_2 (the 2-local unitary after the RESET gate). In other words, we set $R_{\alpha} = R_{\beta}$ and $R_{\delta} = R_{\gamma}$.

The parameters we used for map-1,2,3 are presented in Table III and Table IV for the even and odd layers, respectively.

	map-1	map-2	map-3
U_1, ϕ_1	-2.63	2.13	0.77
U_1, ϕ_2	1.71	-1.31	-2.46
U_1, ϕ_3	0.21	-0.71	2.59
U_2, ϕ_1	-1.07	-2.07	-0.79
U_2, ϕ_2	-2.12	-1.12	1.09
U_2, ϕ_3	2.73	-2.73	-1.80

TABLE III. Rotation angles used to define the RESU gates in the three simulated deterministic maps, for the even layer. The angles are given in radians.

	map-1	map-2	map-3
U_1, ϕ_1	1.42	-2.32	2.57
U_1, ϕ_2	-2.92	1.92	3.04
U_1, ϕ_3	-0.33	-0.73	2.67
U_2, ϕ_1	2.83	-2.83	-2.72
U_2, ϕ_2	1.36	1.87	-1.79
U_2, ϕ_3	-1.08	-1.98	0.21

TABLE IV. Rotation angles used to define the RESU gates in the three simulated deterministic maps, for the odd layer. The angles are given in radians.

2. Noise model in the deterministic case

In the deterministic case, we used a more expressive noise model than was used in the stochastic case, since we wanted the same model to describe also the real quantum hardware experiments of Sec. VI. For each qubit, we used 7 noise parameters: $\theta_x, \theta_y, \theta_z$, to model depolarization in the $\hat{x}, \hat{y}, \hat{z}$ directions, $\theta_{amp}, \theta_{ex}$ to model general amplitude damping noise, and θ_0, θ_1 to model the noisy RESET gate (as was done in the stochastic case).

The depolarization noise channels in the different directions were modeled by the Lindbladians

$$\mathcal{L}_{\sigma}(\rho) \stackrel{\text{def}}{=} \sigma \rho \sigma - \rho, \qquad \sigma \in \{X, Y, Z\},$$
 (C1)

For the generalized amplitude damping channel [52, 53], we used the Lindbladian

$$\theta_{amp}[(1-\theta_{ex})\mathcal{L}_{amp,+}+\theta_{ex}\mathcal{L}_{amp,-}],$$

where

$$\mathcal{L}_{amp,\pm}(\rho) \stackrel{\text{def}}{=} \sigma_{\pm}\rho\sigma_{\mp} - \frac{1}{2} \{\sigma_{\mp}\sigma_{\pm}, \rho\}.$$
 (C2)

Physically, the θ_{amp} models the strength of the general amplitude damping process, and θ_{ex} models the occupation of the qubit's state $|1\rangle$ at thermal equilibrium. The simple amplitude damping model is described by $\mathcal{L}_{amp,+}$, which corresponds $\theta_{ex} = 0$, where the equilibrium state of the qubit is assumed to be $|0\rangle\langle 0|$ (which correspond to a qubit at zero temperature).

In the numerical simulations we chose the dimensionless noise parameters $\{\theta_x, \theta_y, \theta_z, \theta_{amp}, \theta_{ex}\}$ randomly between the values of 0.04 and 0.1. The θ_0, θ_1 parameters for the noisy RESET were randomly generated between the values 0.87 and 0.98, as in the stochastic case.

In our numerical simulations we have used several randomly generated gate durations using the same bounds as for the stochastic map, given in Appendix B 3. The resulting time scale T_0 was approximately $4 \, [\mu sec]$.

Appendix D: Details of the quantum device noise model characterization results

Details of the readout error mitigation scheme for k-local Paulis

For quantum readout error mitigation (QREM), we followed the approach of Ref. [56], but adapted it to k-local readout statistics obtained using the overlapping local tomography from Ref. [8]. The method empirically evaluates the conditional probability distribution $P(\underline{x}|\underline{y})$ of measuring $\underline{x} = (x_1, \ldots, x_k)$ classical bit string in standard basis after the system is prepared the quantum state $|\underline{y}\rangle\langle\underline{y}|$ for $\underline{y} = (y_1, \ldots, y_k)$. In our case, we used k=4 for learning the noise channel (part (ii) in Sec. VIA) and k=2 for testing our characterization

(part (iii) in Sec. VI A). In the ideal case, $P(\cdot|\cdot)$ is a Kronecker delta-function. Upon obtaining the $P(\cdot|\cdot)$, we used to 'fix' an empirical probability $P_{noisy}(\underline{x})$ of measuring \underline{x} in the computational basis, as follows. Assuming that $P_{noisy}(\underline{x}) = \sum_{\underline{y}} P(\underline{x}|\underline{y}) \cdot P_{ideal}(\underline{y})$, we extracted $P_{ideal}(\underline{x})$ by

$$P_{ideal}(\underline{x}) = \sum_{\underline{y}} P^{-1}(\underline{x}|\underline{y}) \cdot P_{noisy}(\underline{y}),$$

where $P^{-1}(\underline{x}|y)$ is the matrix inverse of $P(\underline{x}|y)$.

2. Estimated noise parameters of the ibm_lagos v1.0.32 device

The experimental results presented in Sec. VIB and Sec. VIC were obtained from the ibm_lagos v1.0.32 quantum device on the IBMQ platform on September 11, 2022. The time scale based on the data from the device backend was $T_0 = 3.584 \, [\mu sec]$.

In Table V, we give the estimated values of the dimensionless noise (coupling strength) parameters $\{\theta_x, \theta_y, \theta_z, \theta_{amp}, \theta_{ex}\}$, which are described in Appendix C 2. The values of 10^{-5} and 0.1 are the lower and the upper bounds on the parameters in the numerical optimization, at which the gradient with respect to the specific parameter is forced to zero as an overall stability measure.

	qubit 0	qubit 1	qubit 2	qubit 3	qubit 4
θ_x	0.1	10^{-5}	10^{-5}	10^{-5}	10^{-5}
θ_y	10^{-5}	0.1	0.1	10^{-5}	10^{-5}
θ_z	10^{-5}	0.1	0.1	10^{-5}	10^{-5}
θ_{amp}	0.0598	0.0377	0.1	10^{-5}	0.0749
θ_{ex}	10^{-5}	0.0961	0.0705	0.000279	10^{-5}

TABLE V. Estimated values of the dimensionless noise parameters.

The estimated values of the θ_0, θ_1 parameters of the noisy RESET gates are given in Table VI (see Eq. (23)

in Sec. IV A). In the optimization, we used 0.99 as an upper bound to θ_0 , θ_1 . We note that for the RESET gate on the qubit 4 the optimization was not performed. This is because in the definition the RESU gate (see Fig. 2) the RESET gate acts on the first qubit in the pair, and so we did not use RESET on qubit 4.

	qubit 0	qubit 1	qubit 2	qubit 3	qubit 4
θ_0	0.926	0.941	0.905	0.99	0.96
θ_1	0.99	0.927	0.929	0.895	0.96

TABLE VI. Estimated values of the RESET gate parameters.

In Table VII, we give the estimated values of CX gate noise parameters, representing the coherent errors in the two-qubit gate (see Eq. (A1) in Appendix A). We note that the θ_3 parameter in the gates $\mathrm{CX}(0 \to 1), \mathrm{CX}(1 \to 2), \mathrm{CX}(2 \to 3), \mathrm{CX}(3 \to 4)$ was not affected by the optimization (i.e., the gradient with respect to θ_3 vanished for these gates), and remained in its ideal inital value of 1.0. In a hindsight, this can be explained by the fact that θ_3 is equivalent to adding a \hat{z} rotation after CX. In the gates $\mathrm{CX}(0 \to 1), \mathrm{CX}(1 \to 2), \mathrm{CX}(2 \to 3), \mathrm{CX}(3 \to 4),$ this rotation is followed by a RESET gate, which is insensitive to phases in the standard basis, and as a result the θ_3 parameter does not affect RESU gate (and therefore it does not affect the steady state).

	θ_1	θ_2	θ_3
$CX(0 \rightarrow 1)$	0.976	1.352	1.0
$CX(1 \rightarrow 0)$	1.053	1.029	0.587
$CX(1 \rightarrow 2)$	0.791	0.711	1.0
$CX(2 \rightarrow 1)$	0.987	1.020	0.936
$CX(2 \rightarrow 3)$			
$CX(3 \rightarrow 2)$			
$CX(3 \rightarrow 4)$			
$CX(4 \rightarrow 3)$	1.062	1.008	1.030
1			

TABLE VII. Estimated values of the CX gate parameters. The notation $\mathrm{CX}(i \to j)$ corresponds to the gate with control qubit i and target qubit j.